ΠΑΝΕΠΙΣΤΗΜΙΟ ΚΡΗΤΗΣ

UNIVERSITY OF CRETE

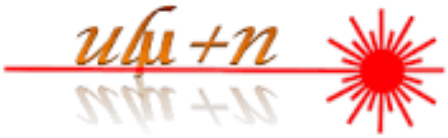

Pulsed laser processing of graphene-based materials

Master Thesis

Andreas Michael

Ph739

Supervisor: Dr.Emmanuel Stratakis

Advisor: Dr.Stella Maragkaki

June 2024

Acknowledgments

I want to thank everyone who helped me complete this master's thesis.

First, I am very grateful to my supervisor, Dr. Emmanuel Stratakis, for giving me the opportunity to work in the Ultrafast Laser Micro and Nano Processing Laboratory (U.L.M.N.P) and be part of this project. Special thanks to my advisor Dr. Stella Maragkaki for always being there when I needed her support, reviewing my progress constantly, and guiding me through my master’s thesis. Her knowledge and encouragement were crucial to this research.

In addition, I would like to thank all the Laser’s processing subgroup members for their outstanding feedback. Further appreciation to all the U.L.M.N.P group members who made working enjoyable and enlightening. Special thanks to Ms. Danai Katrisioti and Dr. Emmanuel Nikoloudakis, who took their time and collaborate for Raman and Elelectrocatalysis measurements. Many thanks to Ms. Aleka Manousaki for the SEM measurements.

Last but not least, I would like to thank my beloved friends and family. All their support and encouragement have been vital to make it through hard times.

Contents

Abstract

In recent years, graphene, due to its exceptional properties, has attracted attention in the research field. Graphene and its derivatives have been extensively used in applications such as energy, sensors, etc. The main objective of this thesis was to investigate the optimal conditions for the reduction of graphene oxide using laser irradiation. The motivation behind this study was the future utilization of reduced graphene oxide in energy-related applications, such as photovoltaic systems and hydrogen production through electrocatalysis.

Initially, a brief description of graphene and its exceptional properties is given. Its structure and preparation methods are described, as well as the reduction of graphene oxide used in this work. Next, graphene oxide is similarly described, along with its reduction methods. At the end of the first section, the basic principles of the characterization methods used in the experimental process are briefly described.

The second section is dedicated to describing the experimental process for the production and study of the final reduced graphene oxide films. Initially, the preparation process of both the initial graphene oxide solution and its deposition on the substrate is recorded. Then, the reduction process is described, using pulsed infrared lasers with three different pulse durations. The study is conducted on films with thicknesses of two hundred and one hundred nanometers. Next, the characterization methods are presented. Finally, a very interesting application for electrocatalytic hydrogen production, using the produced films, is briefly described.

The final results are summarized in the last section, where the optimal reduction conditions for the different pulse durations and the two discussed thicknesses are presented. The results were captured through various spectroscopy measurements, electrical measurements, and microscopy images. Finally, results from the electrocatalytic hydrogen production are presented.

Περίληψη

Εδώ και κάποια χρόνια, το γραφένιο, λόγω των εξαιρετικών του ιδιοτήτων έχει τραβήξει την προσοχή στον ερευνητικό τομέα. Το γραφένιο, όπως και παράγωγά του έχουν χρησιμοποιηθεί κατά κόρων σε εφαρμογές όπως ενέργεια, αισθητήρες κτλ. Ο κύριος στόχος της παρούσας διπλωματικής εργασίας ήταν να διερευνηθούν οι βέλτιστες συνθήκες αναγωγής του οξειδίου του γραφενίου μέσω χρήσης ακτινοβολίας λέιζερ. Το κίνητρο πίσω από αυτή τη μελέτη ήταν η μελλοντική αξιοποίηση του ανηγμένου γραφενίου σε εφαρμογές που σχετίζονται με την ενέργεια, όπως τα φωτοβολταϊκά συστήματα και η παραγωγή υδρογόνου μέσω ηλεκτροκατάλυσης.

Αρχικά, γίνεται μια σύντομη περιγραφή για το γραφένιο και τις εξαιρετικές του ιδιότητες. Περιγράφεται η δομή του καθώς και οι μέθοδοι παρασκευής του, όπως φυσικά και η αναγωγή του οξειδίου του γραφενίου που χρησιμοποιείται σε αυτή την εργασία. Στην συνέχεια περιγράφεται αντίστοιχα και το οξείδιο του γραφενίου, καθώς και οι μέθοδοι αναγωγής του. Στο τέλος της πρώτης ενότητας περιγράφονται σύντομα βασικές αρχές των μεθόδων χαρακτηρισμού που χρησιμοποιήθηκαν στην πειραματική διαδικασία.

Η δεύτερη ενότητα αφιερώνεται στην περιγραφή της πειραματικής διαδικασίας για την παραγωγή και μελέτη των τελικών υμενίων ανηγμένου οξειδίου του γραφενίου. Αρχικά καταγράφεται η διαδικασία παρασκευής τόσο του αρχικού διαλύματος οξειδίου του γραφενίου καθώς και της εναπόθεσης του πάνω στο υπόστρωμα. Κατόπιν, περιγράφεται η διαδικασία αναγωγής του, με χρήση υπέρυθρων παλμικών λέιζερ σε τρεις διαφορετικές διάρκειες παλμών. Η μελέτη γίνεται σε πάχος υμενίων διακοσίων και εκατό νανομέτρων. Στην συνέχεια, παρουσιάζονται οι μέθοδοι χαρακτηρισμού. Τέλος, περιγράφεται σύντομα μια πολύ ενδιαφέρουσα εφαρμογή για ηλεκτροκαταλυτική παραγωγή υδρογόνου, με την χρήση των παράγωγων υμενίων.

Τα τελικά αποτελέσματα συνοψίζονται στην τελευταία ενότητα, όπου παρουσιάζονται οι βέλτιστες συνθήκες αναγωγής για τους διαφορετικής διάρκειας παλμούς, για τα δύο πάχη που συζητήθηκαν. Τα αποτελέσματα αποτυπώθηκαν με διαφορετικές μετρήσεις φασματοσκοπίας, ηλεκτρικές μετρήσεις και εικόνες από μικροσκοπία. Τέλος, παρατίθενται αποτελέσματα από την ηλεκτροκαταλυτική παραγωγή υδρογόνου.

Chapter 1: Introduction

Graphene

Structure

Graphene is an extraordinary material with very interesting properties attracting interest in the scientific world. Graphene and graphene-based materials have been reported in many scientific papers including several applications like in energy, sensing, storage etc.

Graphene was first discovered by Konstantine Novoselov and Andre Geim in 2004 at the university of Manchester using the famous Scotch tape method. Graphene name originates from the Greek word "graphein," the Greek word for write.[1] As mentioned above, graphene has some extraordinary properties such as:

- Large theoretical specific surface aera (2630 $m^2 g^{-1}$)
- Very high intrinsic carrier mobility (200.000 $cm^2V^{-1}K^{-1}$)
- High thermal conductivity (~ 5000 $Wm^{-1}K^{-1}$)
- Good electrical conductivity (Sheet resistance ~30Ω/sq)
- High Young's modulus (~ 1.0 TPa)
- High optical transmittance (97.7%)

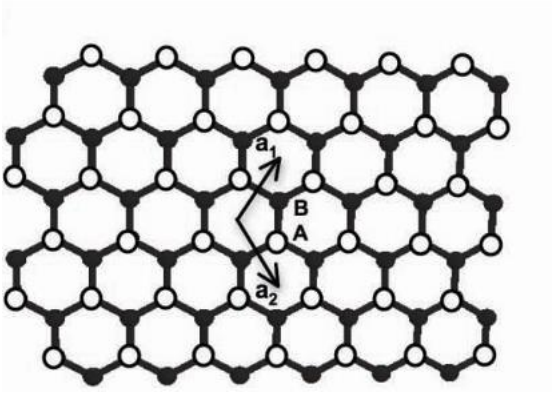

Figure 1 Crystal structure of graphene[1]

The graphene lattice is composed of two sublattices of carbon atoms in a honeycomb crystal lattice[1] (see Figure 1,2).

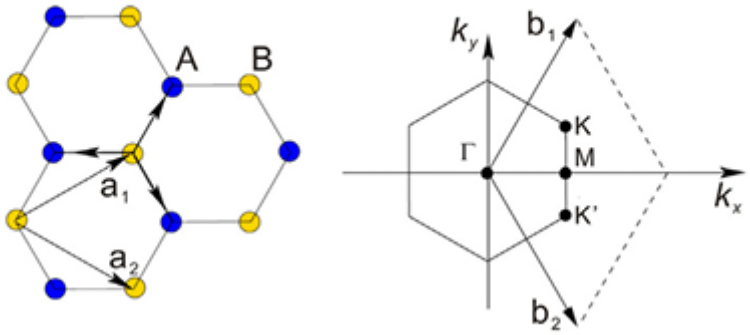

Figure 2 Lattice vectors and Brillouin zone of graphene[2]

The unit cell of graphene can be described by the 2D vectors $\mathbf{a}_1$, $\mathbf{a}_2$, where $\mathbf{a}_1=\frac{a}{2}\left(3,\sqrt{\{3\}}\right)$, $\mathbf{a}_2=\frac{a}{2}\left(3,-\sqrt{\{3\}}\right)$, a=1.42Å.

The reciprocal lattice vectors are $\mathbf{b}_1=\frac{2\pi}{3a}\left(1,\sqrt{\{3\}}\right)$, $\mathbf{b}_2=\frac{2\pi}{3a}\left(1,-\sqrt{\{3\}}\right)$.

Defining those vectors, we can highlight three high symmetry points in the first Brillouin zone of graphene, which are **M, K, K'.** The two last points, which are known as Dirac points, are where the band crossing occurs.

$\mathbf{M}=\frac{2\pi}{3a}(1,0)$, $\mathbf{K}=\frac{2\pi}{3a}\left(1,\sqrt{\{3\}}\right)$. $\mathbf{K'}=\frac{2\pi}{3a}\left(1,-\sqrt{\{3\}}\right)$.

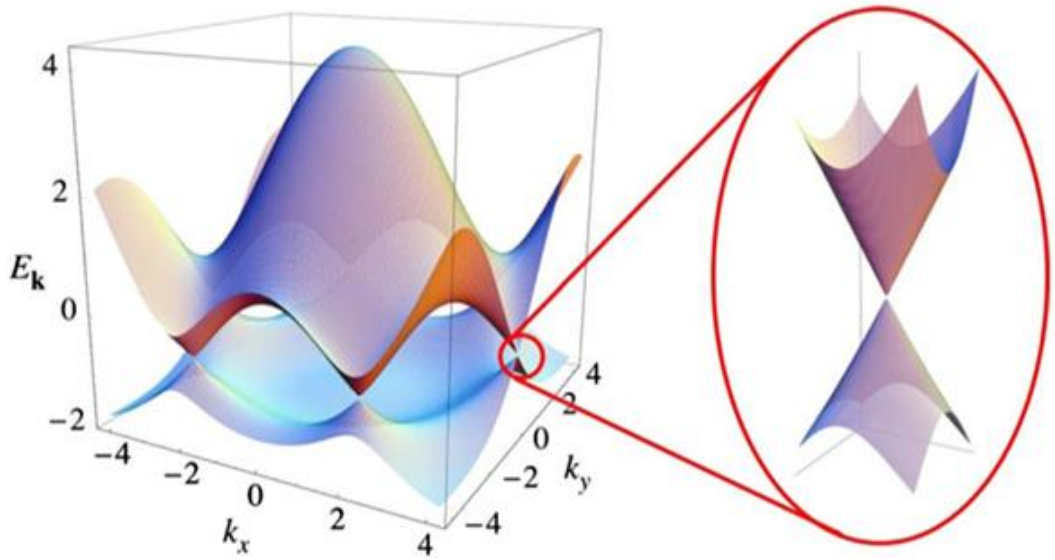

Figure 3 Electronic band structure of graphene[2]

In Figure 3 we see the first Brillouin zone and band structure of graphene. The vertical and horizontal axis represent the energy and the momentum space in the graphene lattice respectively. Electrons in the valence band are tightly bound to the ions in graphene, and the crystalline orbitals are not notably altered from the atomic orbitals. Therefore, the tight-binding model can describe the electronic structure

of graphene, where the lattice symmetry is included as a periodic perturbation of the electrons occupying the atomic orbitals.

The sp^2 hybridized states form fully occupied σ and fully empty σ* bands, with energy gap ~12eV, while the π π* states form a single band with conical self-crossing points at K and K' at the corners of the Brillouin zone[2]. As we can see in Figure 3, the band structure features a linear dispersion at the fermi level. This linear dispersion is responsible for these extraordinary electronic properties of graphene.

Due to the high gap between σ and σ * bands (12 eV), we can simplify the tight-bonding problem by considering that electrons can hop between one or two near p_z orbitals in the electronic Hamiltonian that is:

$$H = -t \sum_{<i,j>.\sigma} \left(\alpha^{+}_{\sigma,\iota} b_{\sigma,j} + H.c.\right) - t' \sum_{<i,j>.\sigma} \left(\alpha^{+}_{\sigma,\iota} a_{\sigma,j} + b^{+}_{\sigma,\iota} b_{\sigma,j} + H.c.\right)$$

α, α^+ are the creation and annihilation quantum operators for electrons with spin σ for the A sublattice and b,b^+ for the B sublattice. t and t' are the hopping parameters for the nearest neighbor orbitals in the A and B sublattices and nearest hopping between the same A or B sublattices, respectively. This model was first introduced in 1947 by Wallace.[2]

Solving the one electron Schrödinger equation, we have the dispersion E(k):

$E_{\pm}(\boldsymbol{k}) = \pm t\sqrt{3 + f(\boldsymbol{k})} - t' f(\boldsymbol{k})$, where k is the wave vector k=(k_x,k_y) and the function

$$f(\boldsymbol{k}) = 2\cos\left(\sqrt{3k_y a}\right) + 4\cos\left(\sqrt{\frac{3}{2}k_y a}\right)\cos\left(\sqrt{\frac{3}{2}k_x a}\right)$$

Typical semiconductors have energy dispersions that can be expanded as $E(k) = \pm\frac{k^2}{2m*}$ at the band edges, where q is the wave vector and m* is the effective mass of electrons/holes at the edge of the band. Relations of effective mass and carrier velocity compared to the energy E are $\frac{1}{m*} = \frac{1}{h^2}\frac{d^2E}{dk^2}$ and $u = \frac{1}{h}\frac{dE}{dk}$. In graphene, the linear dispersion near the Fermi level, reveals the "massless" Dirac fermions, where the relation of E-k is known as the Dirac cone and K, K' as the Dirac points. The E-k relation near the Dirac points is:

$E_{\pm}(k) = \pm u_F|k| + 0\left(\frac{\mathrm{k}}{\mathrm{K}}\right)^2$, $u_F = 3a\frac{t}{2} \sim 10^6\frac{m}{s}$ the fermi velocity of electronic states at the fermi surface. Having linear dispersion results in ultrarelativistic particles that are quantume mechanically described by the Dirac equations.[2]

Concluding, graphene can be differentiated from other mainstream semiconductors due to[3]:

- Zero band gap opposing to typical finite band gaps. Electrons change to holes at the Dirac points or vice-versa. In addition, Fermi level is always in Valence or Conduction band, while in typical semiconductors can be in the energy bandgap.
- Linear energy dispersion provides extraordinary electronic properties.
- Graphene is very thin (thickness of a carbon atom ~3 Å). 2D electron gas can be around 5-50nm thickness
- Graphene has finite minimum conductivity

Synthesis

As previously mentioned, graphene was first isolated by Novoselov and Geim in 2004 by using the famous Scotch tape method. Scotch tape method can produce samples with high quality, high carrier mobility, surpassing other methods even up to date. However, it is not the most optimal method to produce graphene as it requires a lot of time for a small quantity produced. Thus, scientists have invented other methods to produce graphene while concerning the scale of production, the quality, consistency, and the cost of the samples.

Methods to produce graphene:[3]

- Mechanical exfoliation
- Thermal Decomposition of SiC
- Chemical Vapor Deposition (CVD)
- Reduction of Graphene Oxide

Mechanical Exfoliation

This method was developed by Novoselov and Geim. Highly oriented pyrolytic graphite is used as a precursor, then subjected to an oxygen plasma etching. Five micrometer deep mesas are created and then pressed into a layer of photoresist, which is then baked the pyrolytic graphite layer was cleaved from the resist. Then, by using scotch tape and peeling thin graphite flakes from the mesas, thin flakes are isolated and released in acetone and captured on a Si/SiO_2 wafer. These flakes are of very high quality and are up to 1mm length as it is shown in Figure 4. These flakes were found to have ballistic transport at room temperature and carrier mobilities up to $15000cm^2V^{-1}s^{-1}$. The downside of this method is the limit of produced size which cannot be increased to use it in the industry.

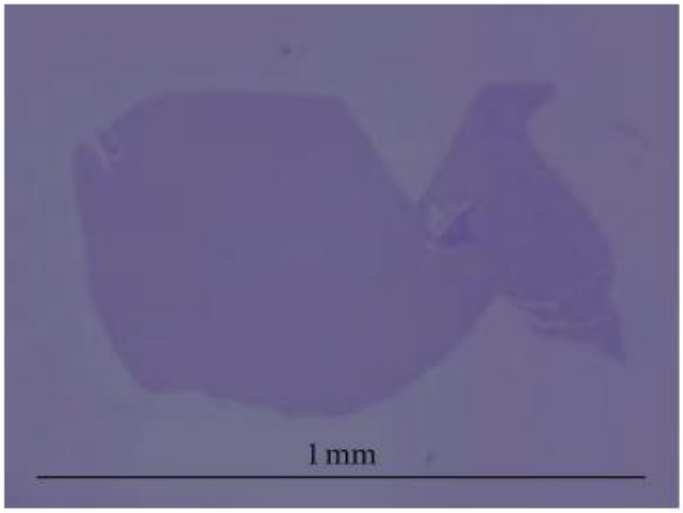

Figure 4 Mechanically exfoliated graphene monolayer[3]

Thermal Decomposition of SiC

Silicon carbide is heated in an ultra-high vacuum chamber (UHV) at high temperatures (1000-1500ºC). At these temperatures, silicon sublimates and carbon atoms are left behind on the surface. In addition, heating SiC in Ar at 900 mbar (by Emtsev et al), produced graphene layers with lower surface roughness, and continuous layers of lengths up to 50μm. This method can produce graphene layers in a wafer-scale, however there are reproducibility issues on larger area growths, difficulties in controlling the number of layers produced as well as the interface effects on the SiC substrate. In Figure 5 we can see an Atomic Force Microscopy (AFM) image of graphene produced by thermal decomposition of SiC.

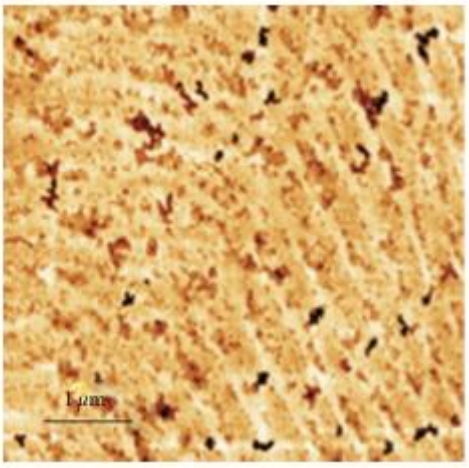

Figure 5 AFM of SiC growth graphene[3]

Chemical Vapor Deposition (CVD)

Opposing to the previous method where carbon was already present in the SiC substrate, in CVD carbon is present in a gas form and grows on a metal substrate. Usually nickel or copper is used, both as a substrate and as a catalyst to graphene growth. The domain size of graphene by CVD is affected by the temperature, methane pressure and flow as it is shown in Figure 6.

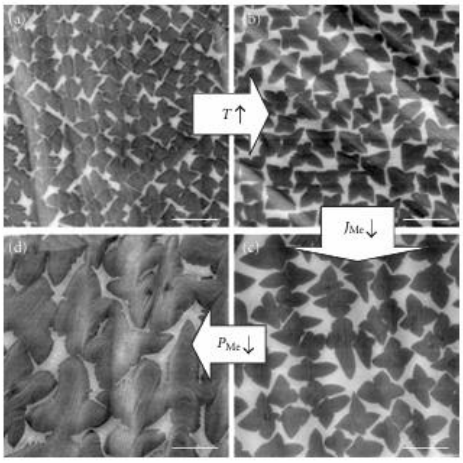

Figure 6 Controlling domain size of CVD graphene[4]

Graphene oxide (GO)

Graphene oxide is used as a precursor to graphene synthesis. GO is first sonicated and reduced so that O and OH groups are removed. During the oxidation process, polar O and OH groups are formed which make it hydrophilic. Thus, it can be exfoliated in several solvents and disperse very well in water. Then GO nanoplatelets are formed by sonicating the GO solution. Following that, the oxygen groups can be removed using several reducing agents such as sodium borohydride, hydrazine etc., or via thermal treatment. In addition, chemical reduction can occur using $NaBH_4$ followed by H_2SO_4 treatment. In this work, photothermal reduction is used to produce reduced graphene oxide, using laser pulses to induce photothermal effects and remove those oxygen groups.[1,3]

Graphene Oxide (GO)

Structure

Graphene oxide is the oxidized form of graphene which is considered as the primary intermediate or precursor to obtain graphene in larger scale, as previously reported. Despite graphene's extraordinary properties, the limit to the large-scale production of single layer graphene emerges the use of GO in academic and industries in the last decades. The simplified structure of GO is that it is a graphene sheet with oxygen attached in the form of carboxyl hydroxyl or epoxy groups on the GO layers[5].Graphene oxide was first investigated by a British chemist B.C Brodie in 1859[6]. He synthesized graphene oxide by adding potassium chlorate ($KClO_3$) to o a slurry of graphite in fuming nitric acid (HNO_3). He observed that the outcome was composed of carbon, hydrogen and oxygen and an increased overall mass. He proposed C:H:O composition to be 61.04:1.85:37.11 and a molecular formula as $C_{2.19}H_{0.80}O_{1.00}$. After heating at 220 ºC, the formula changed to 80.13:0.58:19.29 and $C_{5.51}H_{0.48}$ $O_{1.00}$.

However, the precise chemical structure of Graphene oxide is yet to be precisely determined. The complexity of the material because it is amorphous, berthollide character, it has nonstoichiometric atomic composition is the main obstacle to clarifying the exact chemical structure. Nevertheless, there are many models directed towards the understanding of the GO structure.

The earliest models proposed regular lattices composed of repeating units. In 1939, Hoffman and Holst proposed a lattice consisting of epoxy groups spreading across the basal planes of graphite (C_2O^{18}) as it is shown in Figure 7. Later, Ruess added hydroxyl groups in the model and altered the basal plane to an sp^3 hybridized structure. He also assumed a repeating unit, however $1/4^{th}$ of the cyclohexenes contained epoxides in the 1,3 positions and were hydroxylated in 4 position, forming a regular lattice. Mermoux proposed a structure that entails C-F bonds through rehybridizing the sp^2 planes to sp^3 cyclohexyl structure. In 1969 Sholz and Boehm removed epoxide and ether groups, substituting regular quinoidal species in a corrugated backbone. In addition, Nakajama and Matsuo assumed a lattice framework akin to poly(dicarbon monofluordide), $(C_2F)_n$ which forms to a stage 2 graphite intercalation compound (GIC).

But the most established model is the one proposed in 1998 by Lerf and Klinowski,[5] which rejects the lattice-based model and relies on nonstoichiometric amorphous alternative. They characterized GO by the ^{13}C and ^{1}H nuclear magnetic resonance (NMR)and found the 60ppm line better related to epoxide groups (1,2-ethers) other than 1,3 ethers, and the 130 ppm line to aromatic entities and conjugated double bonds. Carbon atoms are attached to OH groups a little distorted to their tetrahedral structure, emerging a partial wrinkling of the layers. A flat carbon grid structure with randomly allocated aromatic regions with unoxidized benzene rings and aliphatic six-membered ring regions is proposed (see Figure 8).

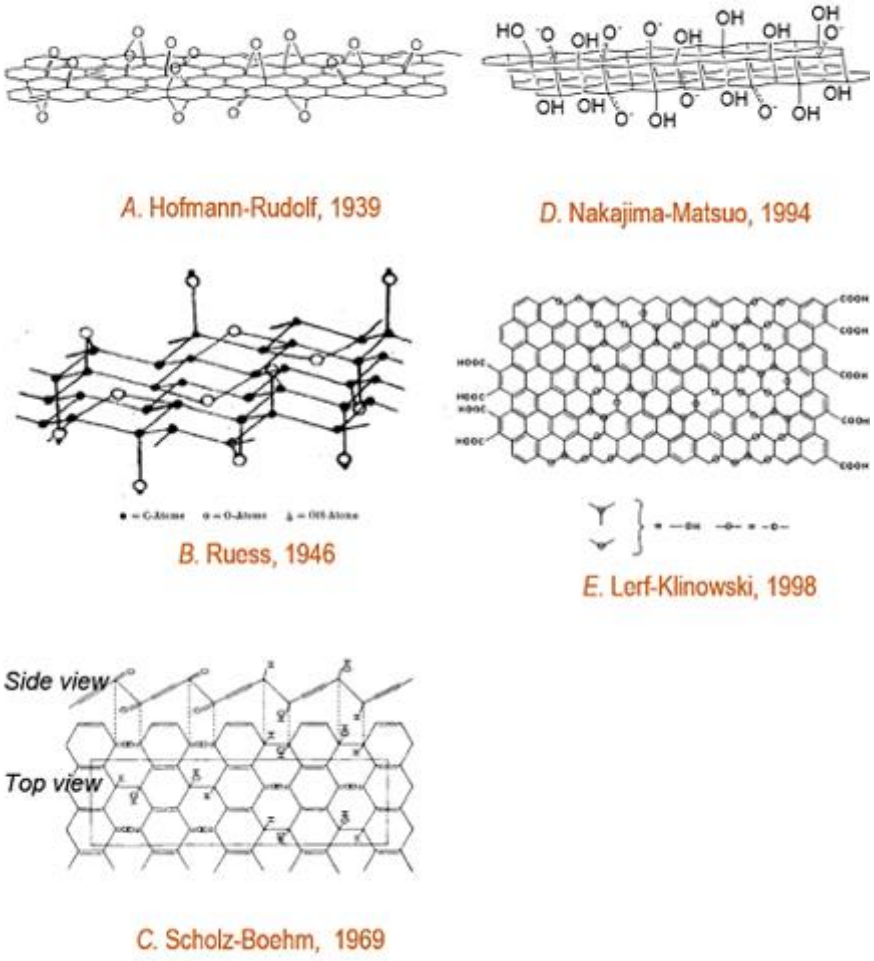

Figure 7 Structure models for GO

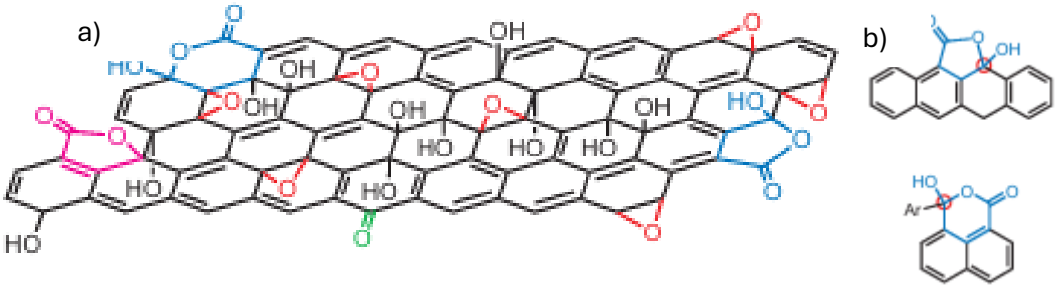

Figure 8 a) New structural model of GO, five and six-membered lactol rings(blue) ester of a tertiary alcohol (purple) hydroxyl (black), expoxy (red) and ketone (green) functionalities), b)five and six-membered lactol rings[7]

Synthesis

Hummers Method[8]

The technique developed by William S. Hummer and Richard E. Offeman involves oxidizing graphite by reacting it with a combination of sulfuric acid (H2SO4), potassium permanganate (KMnO4), and sodium nitrate (NaNO3). In this method, 100g of graphite flakes are mixed with 50g of sodium nitrate and 2.3L of 66° Be sulfuric acid in a jar chilled in an ice bath at 0°C. The mixture is stirred vigorously, and 300g of potassium permanganate is gradually added to avoid a temperature rise above 20°C. Later, the suspension is heated to 35°C for 30 minutes while thickening in the process. Water is slowly incorporated, leading to effervescence and a temperature increase to 98°C. The suspension has a brown color. Following a 15-minute maintenance at 98°C, the suspension is diluted with 14L of warm water and treated with 3% hydrogen peroxide until it transforms into a bright yellow color. Subsequent filtration, washing with warm water, and dispersion in 32L of water result in a mixture with approximately 0.5% solids. The process concludes with the production of dry graphite oxide through centrifugation and dehydration at 40°C over phosphorous pentoxide in a vacuum.

Figure 9 Bright yellow solution[9]

Improved Hummers Method[10]

The revised method involves excluding sodium nitrate from the reaction formula. Initially, 3g of graphite powder is introduced to 70 mL of concentrated H_2SO_4 and agitated in an ice bath. Subsequently, $KMnO_4$ is slowly integrated to maintain low temperatures. The suspension is then transferred to an oil bath and stirred for 30 minutes. Following this, 150 mL of water is added and stirred for 15 minutes at 95°C. Further additions include 500mL of water and 15mL of H_2O_2 (30%), resulting in a color change from dark brown to yellow. After filtration and washing with 250mL aqueous HCl solution to eliminate metal ions, the resultant solid is air-dried and subsequently diluted to 600mL to form a graphite oxide aqueous dispersion. To eliminate residual metal species, the dispersion undergoes purification through dialysis for a week. Finally, it is further diluted to 1.2 L, stirred overnight, and sonicated for 30 minutes to achieve Graphene oxide exfoliation. The resulting GO dispersion is centrifuged for 40 minutes to eliminate unexfoliated GO. This improved version of Hummers' method eliminates the generation of hazardous gases, simplifies the waste liquid purification process, and reduces the overall cost of Graphene oxide synthesis.

Reduction of Graphene oxide

As previously mentioned, GO is the oxidized form of graphene containing hydrophilic functional groups. Functional groups like hydroxyl epoxy carbonyl and carboxyl need to be removed to restore the intrinsic graphene properties. The sp^2 disrupted bonding networks make graphene oxide an insulator, so they need to be removed. There have been many methods proposed to induce the graphene oxide reduction, like chemical, thermal, photo-induced etc. [11,12]

Chemical reduction

The most popular chemical reductant used has been hydrazine monohydrate ($N_2H_4H_20$). The first example presented by hydrazine was reported in 2007 by Stankovich et al. The hydrazine reacts with epoxy groups in Go to form hydrazino alcohols and amino aziridine moieties which can thermal eliminate di-imide and form carbon-carbon double bonds. The liquid reactant can be added to the GO aqueous dispersion which provides an accumulated graphene-based nanosheets. When dried, the product obtained is a black powder with increased conductivity. This method is a promising approach for a large-scale production, but some alternative green reducing agents could be valuable in the future.[13]

Thermal reduction

Graphene oxide can be reduced by thermal annealing. In the early stages of graphene research, in order to obtain graphene, graphite oxide was exfoliated by rapid heating(>2000ºC). The oxygen functional groups can be decomposed into CO or CO_2 gases. However, this process can produce only small sized wrinkled graphene sheets. When the functional groups are detached from the carbon plane, they can remove some carbon atoms and result in some distortion of the carbon plane. These defects can decrease the ballistic transport, the carrier mobility, and the conductivity of the graphene sheets.[11]. A different way to thermal annealing is to exfoliate graphite oxide in the liquid phase. The reduction level is dependent on the heating temperature as it is shown in Figure 10. In addition, thermal annealing is also dependent on the annealing atmosphere. The main setback of thermal annealing is the high temperatures needed to thermally reduce, meaning in high energy consumptions. In addition, temperature increase must be slow, so that the GO structure will not explode (like the exfoliation of graphite oxide) due to heat expansion, so the whole process is time-consuming.

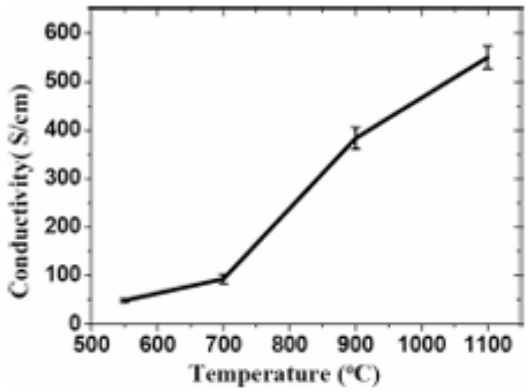

Figure 10 Conductivity as a function of the temperature

Laser reduction of graphene oxide

This method provides a fast and green method to produce reduced graphene oxide sheets with controllable reduction process without using any chemical reducing agents or providing high temperatures[14]. Thus, low cost, high efficiency, adjustable degree of reduction and a flexible patterning for device fabrication is achieved. Light sources like a Xenon Lamp have been used in the past to induce photo-reduction of graphene oxide. The removal of the oxygen containing groups can be either photothermal or photochemical induced, depending on the photon energy provided by the light source [15]. There is a photon energy threshold of 3.2 eV, where for photon energies above the threshold, reduction would undergo photochemical processes, while below the threshold, photothermal reduction occurs. However, in the case of a tightly focused ultra-fast laser beam, multiphoton absorption may occur, so that the GO reduction can undergo both photothermal and photochemical effects process.

It is proposed that photochemical reduction is a process that the photons interact with the chemical bonds such as C−O or C=O and remove the oxygen groups on the surface [1617]. The photo-thermal reduction results from the localized high temperatures, which remove the oxygen functional groups. Then follows a thermally mediated relaxation of the carbon lattice to a planar, hexagonal sp^2 conjugated, graphene-like layer. The energy provided to lattice by heating is required to rearrange into graphene-like domains. Essentially, this is a highly localized, laser-induced, thermal annealing process.

Application field	Photoreduction strategy		
	Light sources	Atmosphere (catalysts)	Mechanism[a)]
Preparation of graphene-like materials	Xenon lamp (300 W)	Solution	PC
	Hg arc lamp (500 W)	Solution (TiO_2)	PC
	High-pressure Hg lamp	Solution ($H_3PW_{12}O_{40}$)	PC
Flexible electrodes	Camera flash	Air, N_2	PT
	Infrared laser (788 nm)	Air	PT
	Femtosecond laser (800 nm)	Air	PT & PC
FETs	Femtosecond laser (790 nm)	Air	PT & PC
	Excimer pulsed laser (248 nm)	Vacuum	PT & PC
	High-pressure Hg lamp	Solution ($H_3PW_{12}O_{40}$)	PC
Gas sensors	Nd:YAG laser (355 nm)	Air	PT & PC
	Hg lamp (500 W)	Solution (WO_3)	PC
Photovoltaic devices	Xe arc lamp (450 W)	Solution (TiO_2)	PC
	Xe lamp (300 W)	Air (TiO_2)	PT & PC
Li-ion batteries	Camera flash	Air	PT
	Xe lamp (1000 W)	Solution (TiO_2)	PC
Supercapacitors	Infrared laser (788 nm)	Air	PT
	Universal X-660 CO_2 laser	Air	PT
Photoignition	Camera flash	Air	PT
Photocatalysis	Xe arc lamp (450 W)	Solution (TiO_2)	PC
	Xe lamp (500 W)	Solution	PC
	Hg lamp (110 mW/cm^2)	Solution (ZnO)	PC
	Xe arc lamp (300 W)	Solution ($BiVO_4$)	PC
	UV spot lamp (50 W)	Solution	PC

Figure 11 Applications of photo-induced rGO and the reduction mechanisms[15]

State of the Art

There have been many papers published regarding the reduction of graphene oxide. Several laser sources with different wavelengths and pulse durations have been used to induce photo-reduction of graphene oxide in solution or film states.

Irradiation wavelength [nm]	Pulse duration	Fluence [mJ cm^{-2}]	Pulse repetition rate [Hz]	Type of laser treatment and treated material
248	20 ns	60–190	1	Patterning/reduction (GO)
248	25 ns	150	1	Patterning/reduction (GO)
248	20 ns	80	1	Patterning/reduction (GO)
532	5 ns	320	10	Patterning/reduction (GO)
532	9 ns	25	20	Patterning/reduction (GO)
790	120 fs	3.5	8×10^7	Patterning/reduction (GO)
800	100 fs	0.057	n/a	Patterning/reduction (GO)
800	120 fs	3.2	8×10^7	Patterning/reduction (GO)
1030	170 fs	50	6×10^4	Patterning/reduction (GO)
1064	10 ps	0.16	10^5	Patterning/reduction (GO)
532	7 ns	100	30	Modification/reduction (GO)
800	120 fs	4	8×10^7	Modification/reduction (GO)
1064	10 ps	3340	10^5	Modification/reduction (GO)
1064	220 ns	400	5×10^4	Modification (GO)
415	10 ns	25 800	10	GO solution reduction

Table 1 Pulsed laser treatment parameters for GO reduction[18]

Rakesh Arul et al. demonstrated the reduction of graphene oxide films by irradiation with three laser sources, a UV (248nm) 5ns laser, an infrared 800nm 100fs laser and a 788nm CW laser[19].

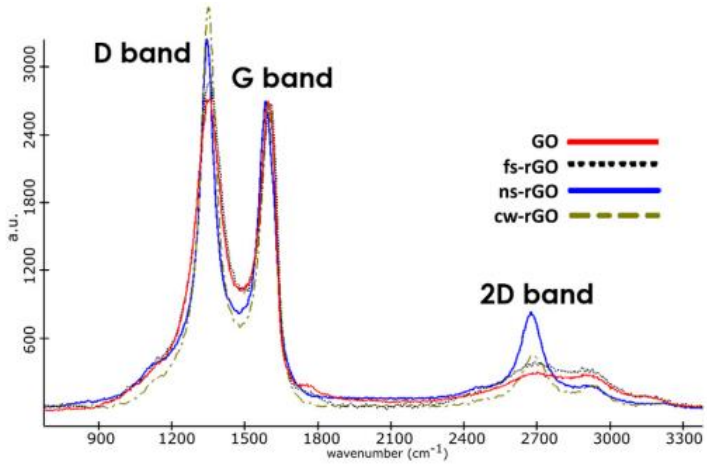

	GO	fs-rGO[a]	ns-rGO	cw-rGO
I_D/I_G	1.0	1.1	1.1	1.3
I_{2D}/I_G	0.10	0.10	0.59	0.17

Figure 12 Raman spectra for GO, ns-rGO,fs-rGO, CW-rGO and their peak ratios[19]

They observed that ns-rGO films (UV ns laser) were the most effective at producing graphene-like films. The IR fs laser removed oxygens from the surface but led to little sp^3 to sp^2 restoration of the surface.

Ayesha Sharif et al in their latest work have successfully fabricated robust flexible sensors by reducing graphene oxide on thin polymer substrates [20]. In their experimental work, they used a 500fs infrared laser, and by controlling the pulses per spot and the energy fluence, they observed drastic decrease in the rGO sheet resistance. Their sheet resistance and Raman ratio results as a function of the energy fluence they used are shown in the Figure below:

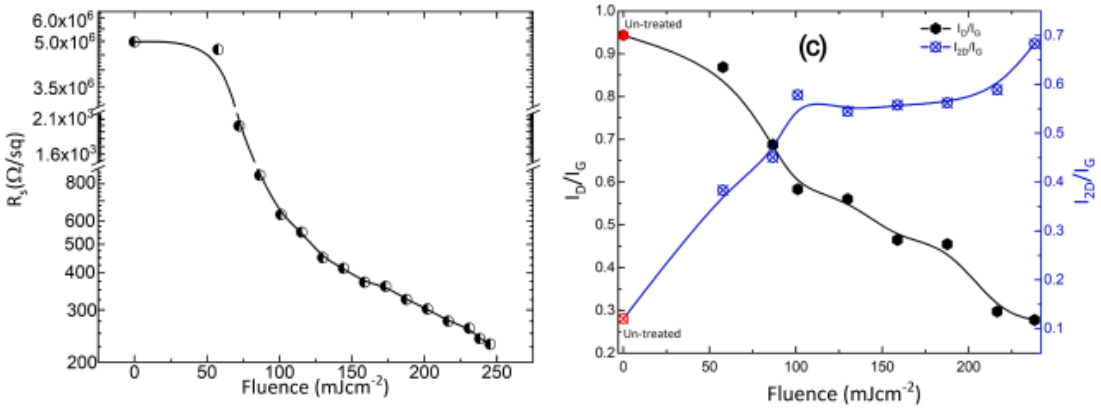

Figure 13 Sheet resistance and Raman peak ratios as a function of Fluence [20]

What we observe is that after the laser treatment, the rGO film shows significant decrease in the sheet resistance compared to the pristine GO film. The I_D/I_G (I_{2D}/I_G) ratio decreases (increases) upon irradiation, which indicates a decrease in the defect densities (some sp^2 domains are restored). Those terms will be extensively described in the next chapter.

In this master thesis, we will examine the pulse duration influence on the GO reduction. We use infrared laser sources to examine the effect of 170fs, 150ps and 1ns pulse duration on the reduction process. In addition, the influence of the film thickness is also examined.

Chapter 2: Materials and Methods

Material preparation:

GO solution

For the preparation of the GO solution, we use Single-Layer graphene oxide Aqueous solution prepared by GRAPHENE SUPERMARKET by the Hummers method. We mix 5mL of GO oxide solution with 15mL distilled water. The initial concentration of the aqueous solution bought is 500mg/L. The product solution is then submerged in a sonicator bath for ten minutes at room temperature, to homogenize the final solution.

Figure 14 Pristine and final GO solution

GO film

As a substrate for the GO film, we use microscope glass. We cut the glass to the desired dimensions using a diamond cutter. Then, the substrates are blown with compressed air to remove glass leftovers. Continuing, the glasses are placed on a holder and submerged in ethanol. Afterwords, the samples are immersed in the sonicator bath for 5 minutes. Finally, they are blasted again with compressed air to evaporate any remaining ethanol.

The next step is to deposit the graphene oxide on the sample. We use a SimCoater Spray coater. The setup consists of a spray coater, a hot plate with XY axis movement, a pump syringe, an ultrasonic generator, compressed air supply and a computer.

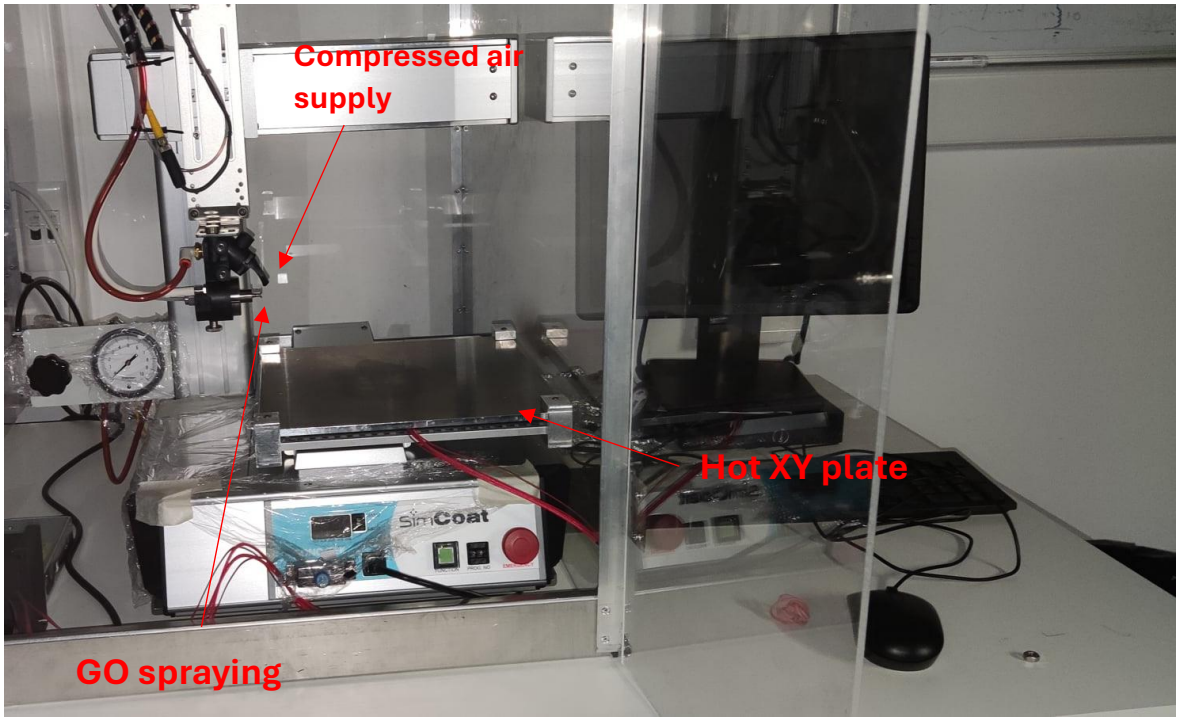

Figure 15 SimCoater spray coater

Figure 16 High accuracy pump syring, ultrasonic generator

The cleaned glass substrates are placed on the XY heated plate and taped with high thermal conductivity tape. Then, the plate is heated up to 100^{o} C. The high accuracy pump syringe is set to provide the Spray coater 0.5mL of GO solution per minute. The pump syringe is connected with the ultrasonic generator so that the GO droplets coming out of the syringe splitting up into tiny droplets in order to have a uniform deposition. When the samples are heated in the desired temperature, we choose the appropriate program on the SimCoater to have the desired GO film thickness. For this work, we prepare 100nm and 200nm GO films.

In a previous work, the spray coater was calibrated to produce a uniform deposition in a 6.5x5cm^2 area. The SimCoater through the computer, runs a pre-loaded pattern (a meander) multiple times(cycles) to produce the GO film. The number of cycles the pattern ran was correlated to the thickness of the film prepared.

Laser reduction of Graphene-oxide films.

As mentioned before, the GO film is an insulator due to its oxygen containing groups. In this work, the reduction of graphene oxide is induced by laser irradiation. The goal of this thesis is to provide a reduced graphene oxide film with good sheet resistance and good optical transparency. In addition, we aim to produce a uniform large area rGO film using an industrial laser. We use two different lasers (IPG and Pharos) so that we cover pulse durations in 3 different regimes (ns, ps, fs). IPG is an Ytterbium picosecond fiber laser (YLPP-1-150x5000-50-M). It has an adjustable pulse duration from 150ps to 5ns and the repetition rate ranges from 30kHz to 1MHz. The experiments of this thesis are performed at 200kHz for 150ps and 1ns. On the other hand, Pharos is a Yb:KGW pulsed laser source (PHAROS SP) producing fs laser pulses with 170fs pulse duration and 200kHz repetition rate.

The experimental setup used is shown in the Figure below:

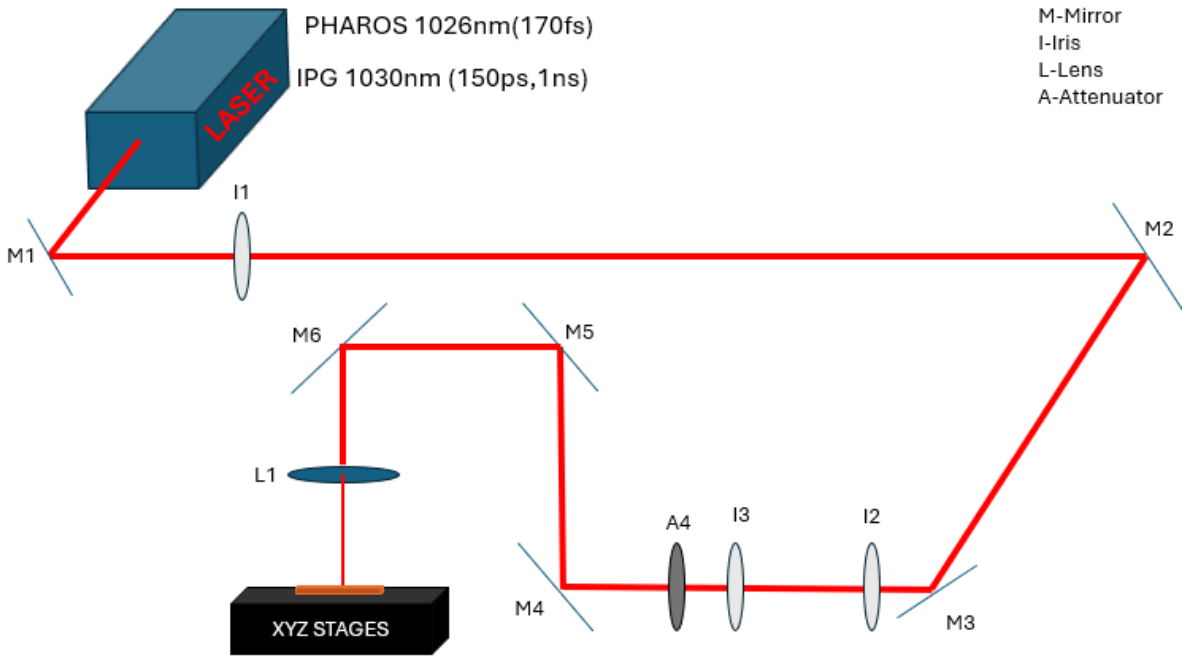

Figure 17 Experimental setup

The laser setup consists of mirrors, a focus lens, and motorized XYZ stages. The laser beam is guided by mirrors and focused on the sample using a focus lens. A 20cm and 15cm focal length lens is used to focus the pharos and IPG laser beam, respectively. The sample is positioned on the beam focus by properly adjusting the Z height on the XYZ stages. Then, the sample is scanned by moving the sample using the XY stage.

The spot diameter is measured as $2w_0$=60μm, $2w_0$=30μm on the focus for the pharos and IPG respectively. The repetition rate used was RR=200kHz for both laser sources. In this work, a parametrization was conducted, changing the number of pulses per spot, energy fluence, pulse duration and the GO film thickness.

The number of pulses per spot is measured as :$PPS = \frac{RR \times d}{u}$, where RR is repetition rate, d is the $2w_0$ at $1/e^2$ of laser spot diameter and u is the scanning speed

The energy fluence is measured as $F = \frac{2P}{RR \times (\frac{\pi d^2}{4})}$, where P is the average laser power as measured by a power meter.

Characterization Methods

After irradiating the samples, we need to characterize them and examine the degree of GO reduction. Methods used in this work are:

- UV-Vis spectroscopy
- Raman spectroscopy
- SEM
- AFM
- 2-probe IV measurement

UV-Vis spectroscopy

Ultraviolet-visible spectroscopy examines the interactions between electromagnetic (EM) radiation in the ultraviolet-visible region and matter[21].

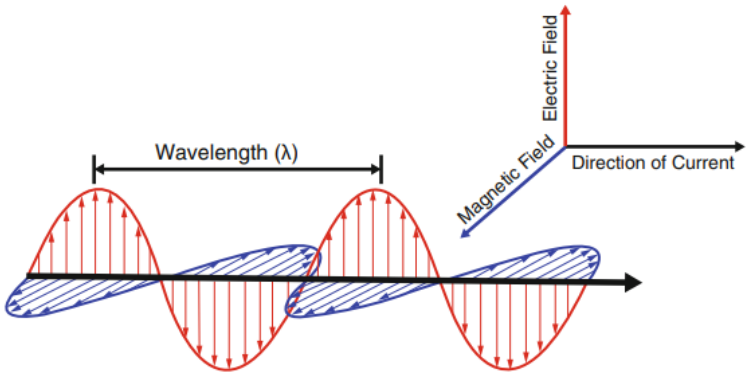

Figure 18 EM radiation schematic[22]

Electromagnetic radiation can interact with matter in different ways such as transmitted, transmitted in a diffuse way, reflected in a specular or diffuse way or absorbed (and maybe emitted as photoluminescence). For the EM radiation to be absorbed, its frequency must correspond to the specific frequency of a transition between two energy levels (Figure19).

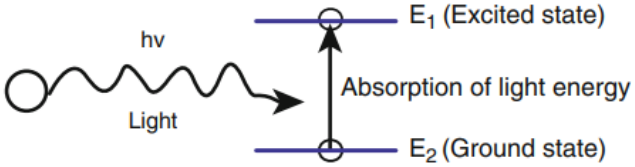

Figure 19 Representation of electronic energy levels

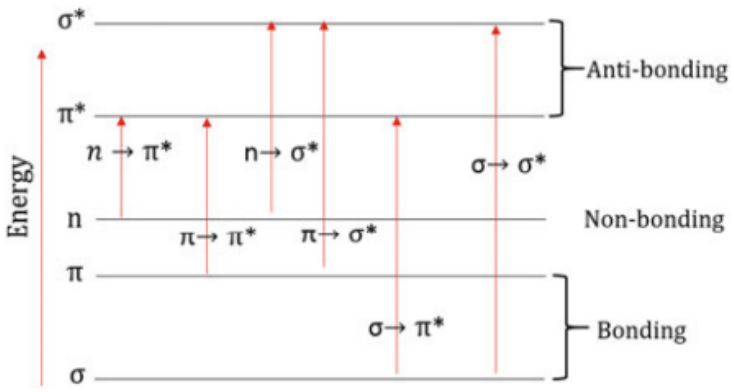

Figure 20 electronic transitions

There are four types of absorption of electronic transitions that are associated with the UV-Vis radiation absorption as it is shown in Figure 20:

1. σ→σ* transition

Bonding to anti-bonding transitions, which require a lot of energy corresponding to the far UV region.

2. π→π* transition

Requires less energy than the previous transition, where double or triple or aromatic rings are contained, thus occurring at a longer wavelength.

3. n→σ* transition

Transitions from the non-bonding to the antibonding orbital require less energy than the first transition. (UV-Vis region)

4. n→π* transition

The non-bonding electrons are held loosely so that the transition requires longer wavelengths.

The energy change of a quantized system when light is absorbed or emitted for wavelength λ is $\Delta E=E_1-E_2=hc/\lambda$, where h is the Plank constant and c is the speed of light. The light absorption on gases and solutions in the UV-Vis region is given by the Bouger-Lambert Beer Law :

$A=ebc=-\log T=\log(I_0/I)$ where A is absorbance, e is molar absorptivity or molar extinction coefficient, b is the thickness c is concentration and T is Transmittance and I_0,I are the light intensities before and after the sample.

For non-apparent samples, the sample presents a total reflection as shown in Figure 21, where R_{total} is the sum of R_S(surface), R_{DS}(diffuse superficial), R_{RD}(retro-diffused) and R_V(diffuse or volume) reflectance.

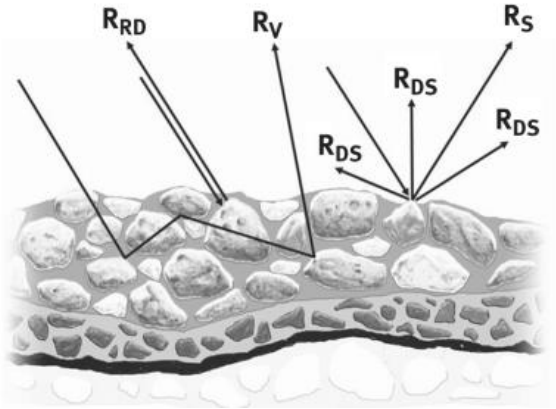

Figure 21 Total reflection modes[21]

Then the absorbance is calculated by : $A(\%)+T(\%)+R_T(\%)=1$ [23]

A typical schematic UV-Vis spectrometer schematic is shown below:

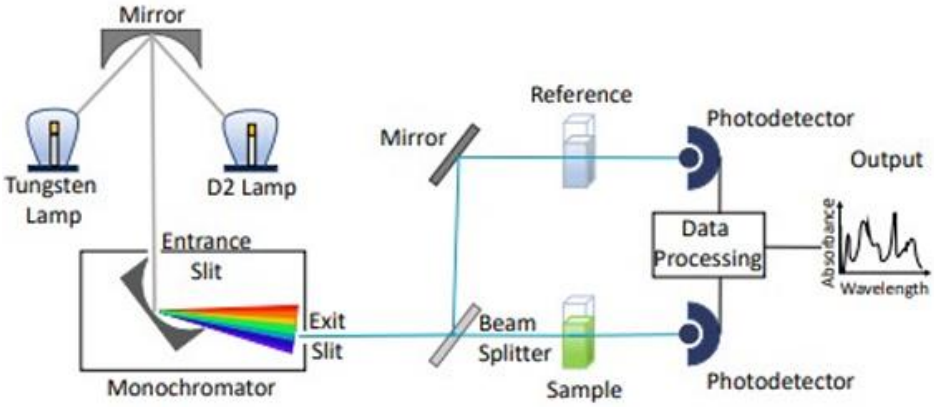

Figure 22 UV-Vis spectrometer

As previously mentioned, UV-Vis spectroscopy measures the light absorbed or transmitted by the sample in the ultraviolet and visible spectrum. The UV-Vis spectrometer used is Duetta HORIBA Scientific.

Figure 23 Duetta Spectrometer[24]

The sample is placed on a holder. To measure the transmittance of the sample, a monochromator is used to scan the light emitted from a Xenon lamp and the light passed through the sample is measured by a photodiode on the other side of the sample (I). Duetta scans again a blank sample (no sample inside) and measures the incident intensity I_0. To calculate transmittance, we use $T=I/I_0 *100\%$.

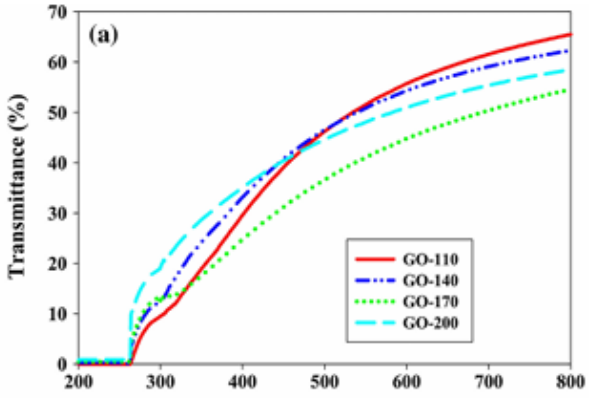

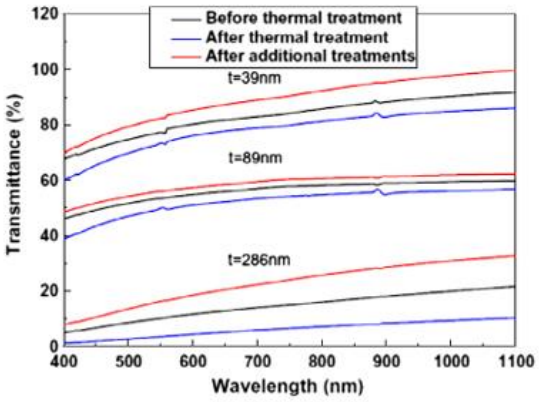

Figure 24 Transmittance spectra of chemically reduced GO[25] *Figure 25 Transmittance spectra of thermally reduced GO*[26]

Raman spectroscopy

Raman spectroscopy is a non-elastic light scattering method, which was named after C.V Raman and K.S. Krismnan who first observed this phenomenon in 1928[27]. They observed that when matter is irradiated with monochromatic radiation, the scattered light includes frequencies different from the initial radiation. A typical Raman spectra is shown in Figure 26.

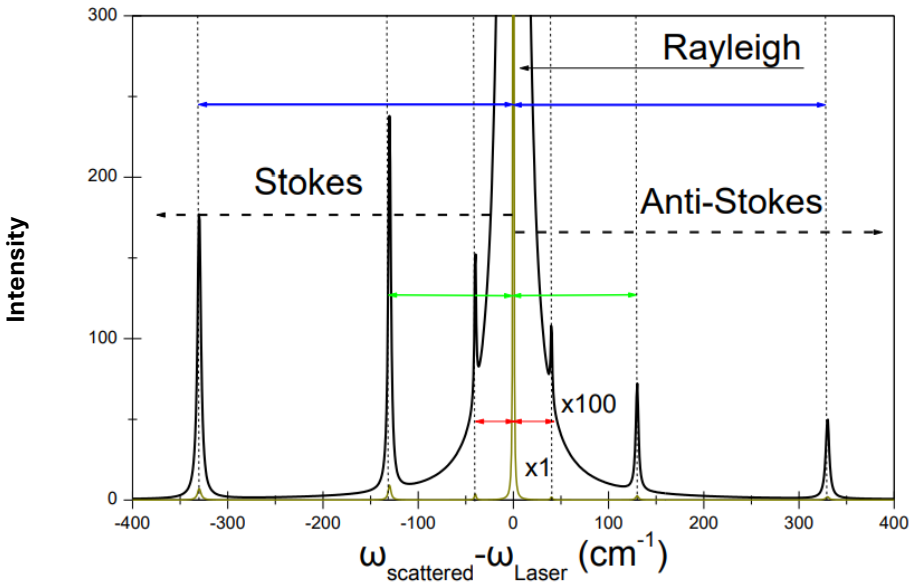

Figure 26 Typical Raman spectra

In Figure 26 we can see the Rayleigh elastic scattering at $\omega_{scattered} = \omega_{laser}$ as well as the non-elastic scattering peaks in frequencies longer and shorter (Stokes and anti-Stokes) than the laser. Stokes and anti-Stokes peaks can be observed as a result of some excitations of the material the light scattered on. These excitations can be either single-particle movements (motion of free electrons or isolated atoms/impurities) or collective (lattice vibrations, plasmons or magnetic moment oscillations). Depending on their interaction with the excitation electromagnetic radiation, classical or quantum description can be interpreted to describe the Raman phenomenon.

Classical approach

In a material, the induced polarization under an electric field is $\vec{P} = \tilde{\alpha}\vec{E}$ where $\tilde{\alpha}$ is the polarizability. The electric field of the electromagnetic wave is $\vec{E} = \vec{E}_0 \sin(\omega_\iota t)$.

If the material executes an internal movement like rotations or vibrations with frequency of the oscillation ω_{01}, the polarizability becomes $\tilde{\alpha} = \tilde{\alpha}_0 + \tilde{\beta}\sin(\omega_{01} t)$ and

$$\vec{P} = \tilde{\alpha}_0 \vec{E}\,\vec{E}_0 \sin(\omega_\iota t) + \frac{\tilde{\beta}\vec{E}_0}{2}[\cos(\omega_\iota - \omega_{01})t - \cos(\omega_\iota + \omega_{01})t]$$

The first term refers to the Raleigh scattering, the second and third term for the stokes and anti-stokes.

Quantum approach

The quantum approach considers that the vibrational energy of a molecule is quantized. Linear molecules have 3N-5 normal vibrations, and non-linear molecules 3N-6. The energy of these vibration states will be: $E_v = \hbar\omega_v\left(v + \frac{1}{2}\right)$, v=0,1,2,3.. the vibrational state.[28]

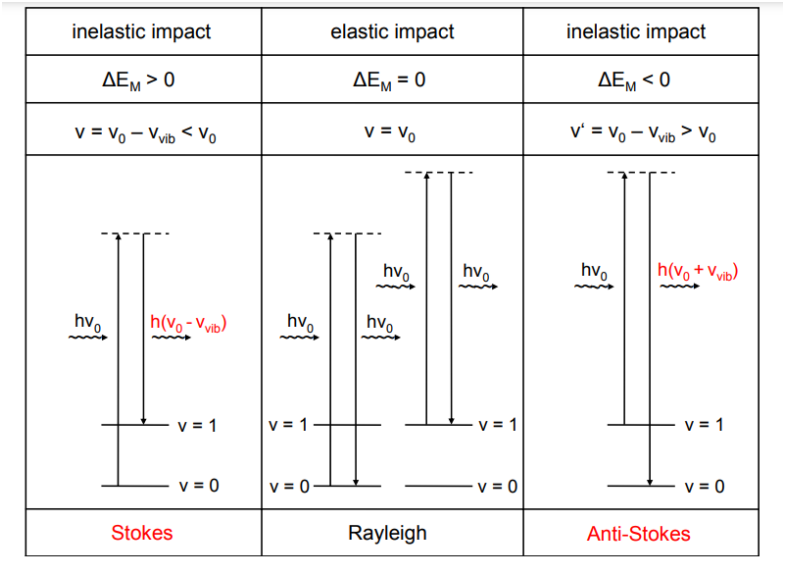

Figure 27 Rayleigh and Stokes/Anti-stokes Raman scattering[29]

The Rayleigh scattering arises from transitions starting and finishing at the same vibrational energy state, Stokes scattering arises from transitions which start from the ground vibrational state and finish ate a higher state and anti-Stokes scattering involves transitions starting from higher vibrational states to a lower state.

At room temperature, most molecular vibrations are in the ground state, which results in higher Stokes scattering probability and less anti-Stoke probability which leads to higher intensity of the Raman Stokes intensity as it is shown in Figure 28. In addition, higher energy of vibrations results in less populated states at any given temperature. Hence, the Stokes Raman scattering is usually examined in Raman Spectroscopy

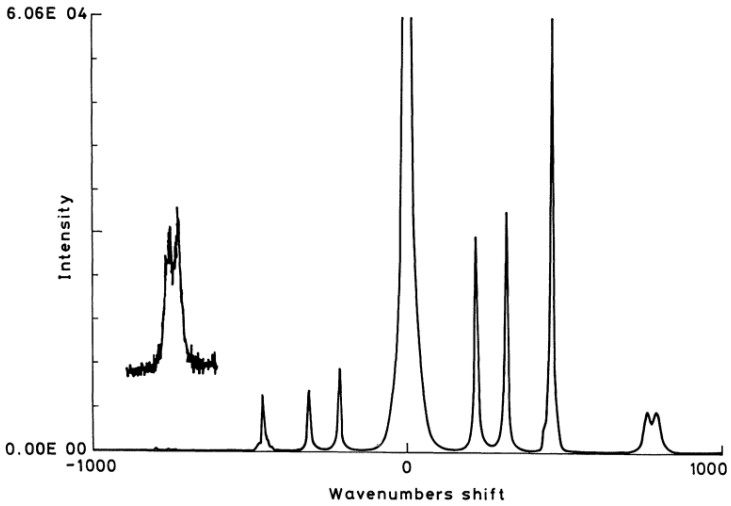

Figure 28 Raman Stokes and anti-Stokes spectrum of carbon tetrachloride, the anti-Stokes at -790cm^{-1} was magnified X100[28]

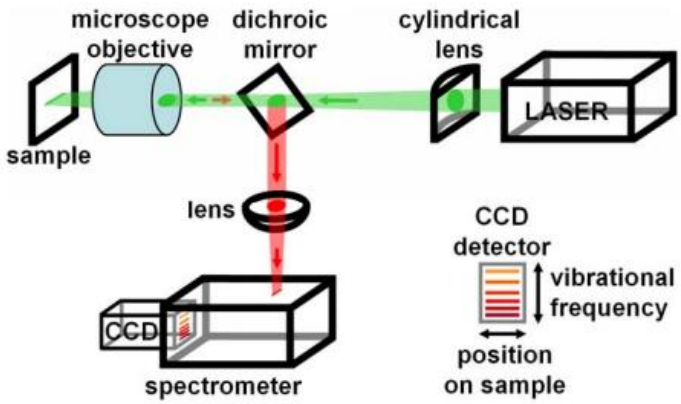

Figure 29 Typical Raman spectrometer[30]

Changing the structure of graphene oxide to reduced graphene oxide by the laser irradiation can be examined by Raman spectroscopy. The characteristic Raman peaks of GO and rGO are at 1354,1580 and 2695 cm^{-1} [31,32] (D,G,2D band peaks) as it is shown in Figure 31. The D vibration band is formed from a breathing modes of sp^2 atoms in rings. The G peak is due to the bond stretching of all pairs of sp^2 atoms in both rings and chains[33]. The last band peak is 2D peak can be used to determine the layers of graphene[34] (see Figure below).

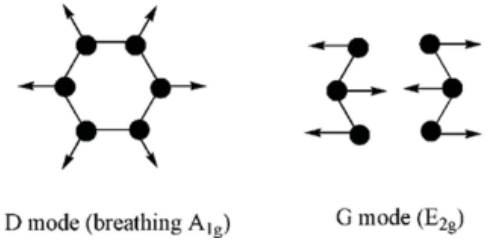

Figure 30 Breathing and stretching modes[18]

The intensity ratio of I_D/I_G measures the lattice disorder degree and average size of sp^2 size domains. In the fs pulse duration case, for low number of laser pulses, a non-thermal ultrafast excitation and removal of oxygen groups takes place, while the lattice order is maintained. Further increasing the number of pulses, thermal effects become dominant, raising photothermal breakage of carbon bonds, introducing some lattice defects[31] (see Figure 32). On the other hand, irradiation with ns pulses, the I_D/I_G increases upon irradiation due to thermal effects.

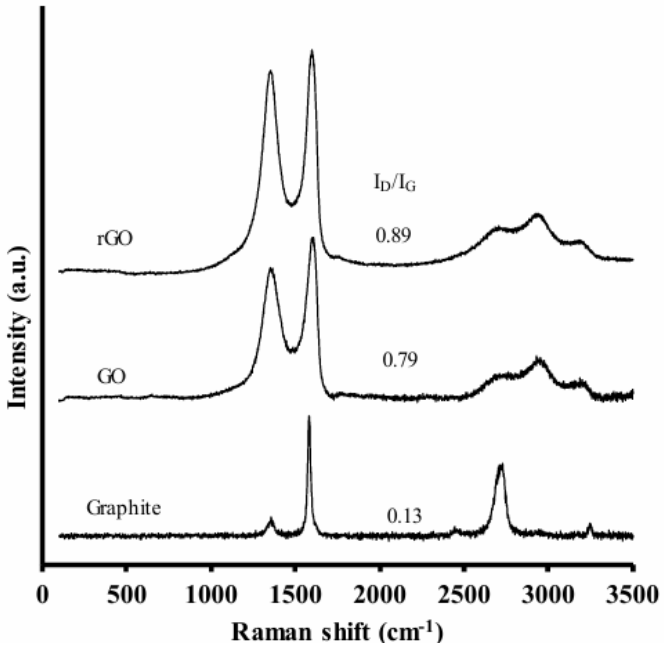

Figure 31 Raman spectra of rGO, GO and Graphite[34]

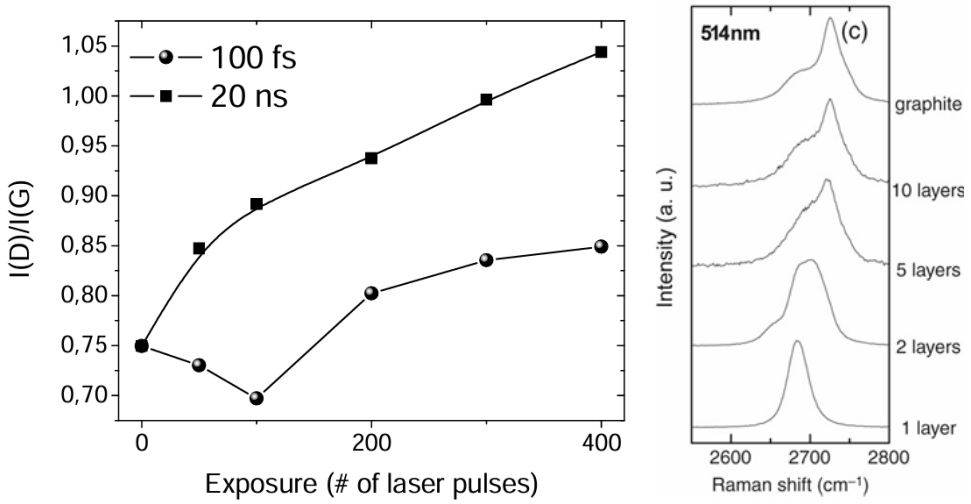

Figure 32 I_D/I_G for100 fs,,20ns pulses[31] *(left), I_{2D} intensity as a function of layers(right)*

Electrical conductivity and Sheet Resistance

Electrical resistance to the flowing electricity is one of the most important electrical characteristics describing a material. Low resistivity means that electrons can easily flow through a material. Electrical conductivity and electrical conductivity are to quantities defined as the inverse of together[35].

In the classical model, we can describe electrical resistance for flowing electricity as the collisions between the free electrons flowing through the material accelerated by an external voltage, with the immobile atoms, as it is shown in Figure 33. The more collisions, the higher the resistivity.

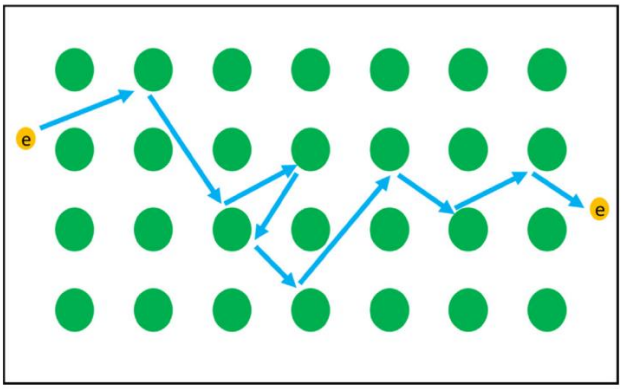

Figure 33 Classical model

Electrical resistivity can be defined by Ohms law E=ρJ, where E is the electrical field, ρ is the resistivity and J is the electrical current density.

In addition, the electric field is proportional to the Voltage as E=V/L, where V is the voltage applied over a distance L.

The current density is defined as J=I/A where I is the electrical current and A is the cross-sectional area where the current flows.

As a result, $V = \frac{I\rho L}{A}$ or $R = \frac{\rho L}{A}$

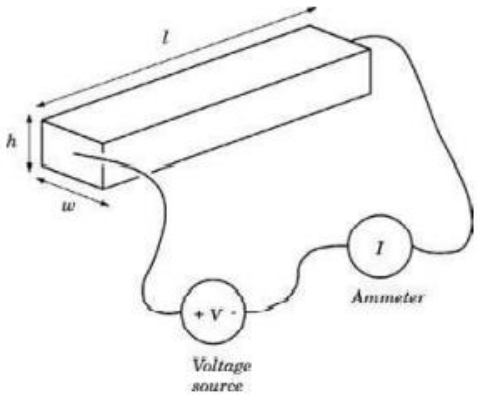

Figure 34 Simple technique for measuring resistivity

Sheet Resistance

Sheet resistance is the resistance measurement across the surface of a material, in contact with the electrodes. The resistivity measured by two-point method is: $\rho = \frac{Rwh}{L}$.

The quantity $\frac{\rho}{h}$ is called Sheet Resistance. When the electrode width is equal to the distance between the electrodes, the resistance measured is equal to the sheet resistance. The unit of Sheet resistance is Ohm per square. Two different-sized squares of the same material have equal sheet resistances.

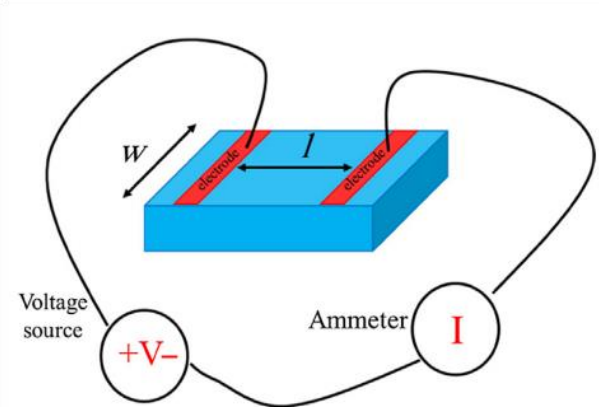

Figure 35 Sheet resistance measurement

Sheet resistance $R_s = Rx\frac{w}{l}$ is the resistance a square film would have (when w=l in Fig.27). The units for sheet resistance are Ohm per square (Ω/sq). Sheet resistance is not dependent on the size of the square film or its thickness. It is fundamentally connected to the material itself. We can consider a rectangular sample as a resistor with resistance R_0 (Figure 36a). Its resistance is equal to its Sheet Resistance as w=l

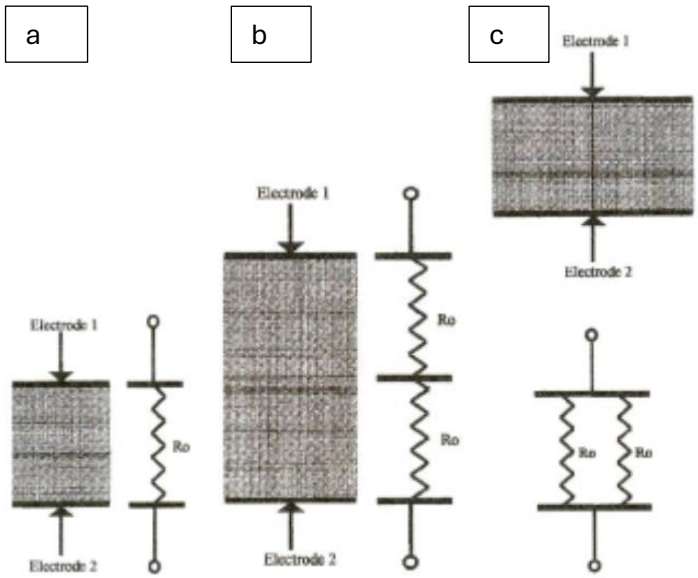

Figure 36 a)Square sample as a resistor, b) rectangular sample (l=2w), c) rectangular sample (w=2l)

Now, consider a rectangular sample which length would be twice its width and resistance equal to 2 R_0. We can consider this as a two-resistor connected in series (Figure 36b)

The measured sheet resistance would be measured as $R_{sheet} = \left(\frac{R_0\, w}{2w} + \frac{R_0\, w}{2w}\right) = R_0$.

Similarly, we can consider a sample with width twice its length (Figure 36c). Its resistance would be $\frac{1}{2}R_0$.

Its sheet resistance would be $R_{sheet} = \frac{1}{\frac{1}{R0}+\frac{1}{R0}}\left(\frac{2l}{l}\right) = R_0$ is still R_0. [36].

Thus, we can conclude that the Sheet resistance of a test sample is equal to the resistance of a square sample regardless of its dimensions.

Sheet Resistance measurement

Upon laser-induced radiation of the GO films, we expect a spectacular decrease of its sheet resistance. We use a two-probe technique to measure the IV characteristics of the samples prepared.

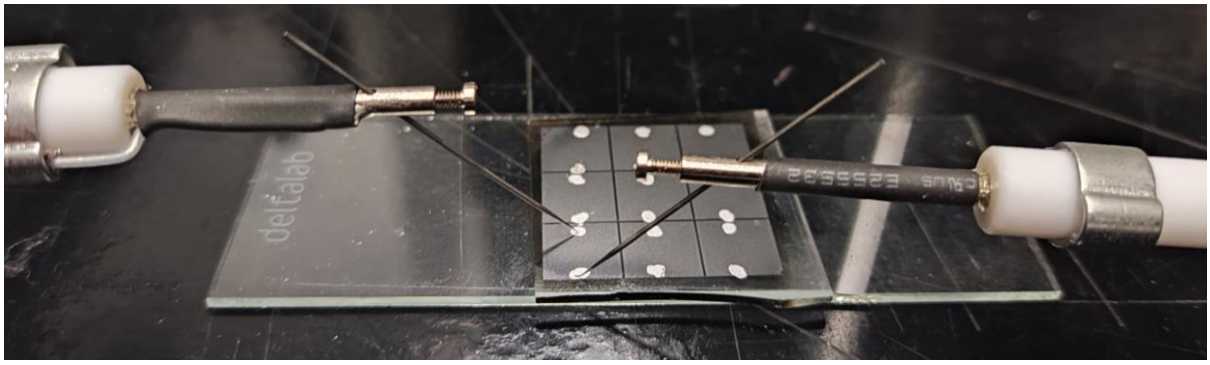

Figure 37 Two probe setup

At first, we apply two drops of super conductive silver paste on the GO and rGO films prepared. The distance between them is precisely measured by a light microscope. Then, we gently place the two probes on top of the silver paint drop to measure their resistance. We can adjust the probes placement in XYZ direction by adjusting the proper screws on the setup.

The two probes are connected to a Keithley parameter analyzer. The analyzer plots the electric current as a function of the applied voltage. The samples resistance is measured from the plot's gradient.

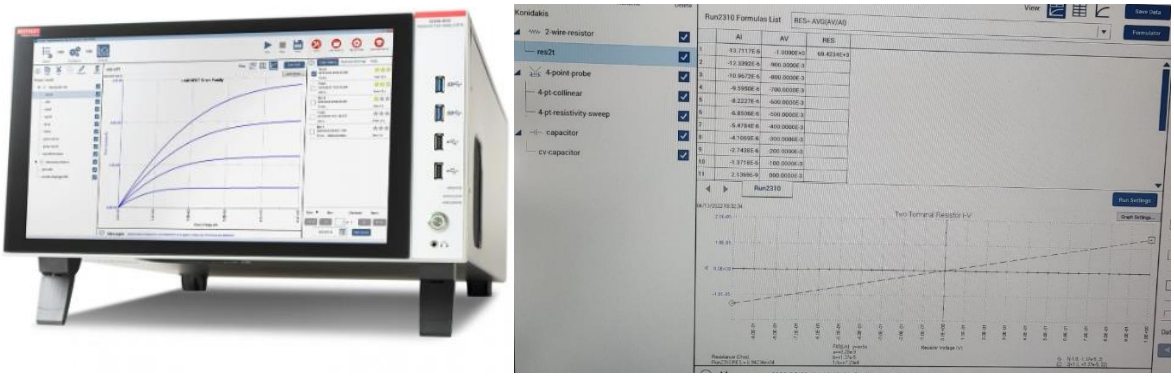

Figure 38 Keithley analyzer and plotted I-V

Scanning Electron Microscopy (SEM)

Using a scanning electron microscope, we can get information about the surface topography, crystalline structure, chemical composition, and electrical behavior of the top of the specimen[37]. Just like the normal microscope, it uses an electron beam instead of light to form images of the sample we examine. However, due to its smaller wavelength, electrons can resolve finer features and details of the surface, much greater than a typical microscope. Today, scanning electron microscopes can magnify objects up to one million times and resolve features up to 1nm in dimension[38].

As Ernst Abbe proved, the image resolution is diffraction limited[39] and can mathematically described by Abbe's equation: $d = \frac{0.612\lambda}{n\,sina}$, d=resolution, λ=wavelength of image radiation, nsina=NA (numerical aperture)

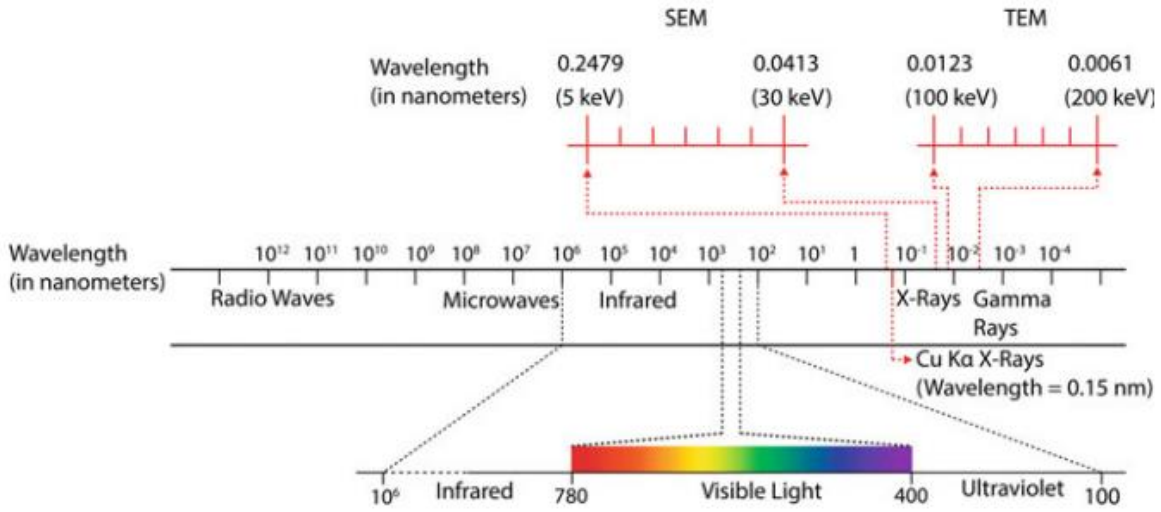

Figure 39 Electromagnetic spectrum, showing the wavelength used in light microscope , SEM and TEM[38]

Hence, by using an electron beam accelerated by a voltage of 100kV, we can achieve a resolution of 0.24nm. In such a way, by adjusting the accelerating voltage applied to the electron beam, we can tune the resolution we need.

The main advantages of imaging with electrons are the very high resolution compared to the normal optical microscope, the very high magnification range they provide (X10-X500,000) and the electron generated signals which can be used to form structural and chemical images of specific areas of the specimen. However, they need vacuum to prevent interactions of electrons with air molecules, and they need very high electron energies, which can sometimes damage the sample examined[40].

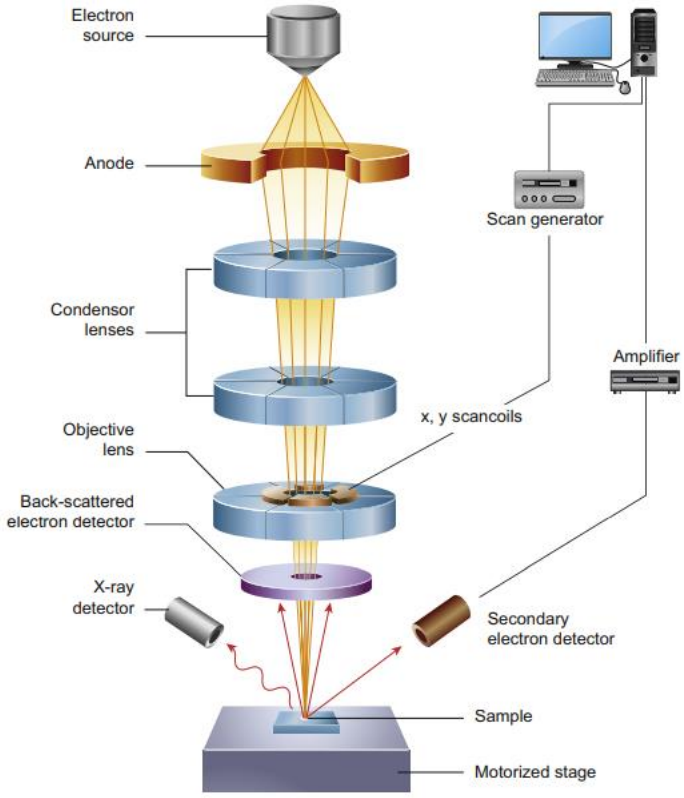

Figure 40 Schematic of a SEM microscope[40]

Atomic Force Microscopy (AFM)

Atomic Force microscopy is another microscopy technique which doesn't require light or electron beam to image sample. It uses a sharp probe touching the surface, building a map of the sample's surface. The main components are the microscope, computer, and control electronics. The microscope contains a scanner (moving the sample or the sharp probe), a force sensor and a sample holder[41].

The three main concepts of AFM are the piezoelectric transducer, the force sensors, and the feedback control. Piezoelectric materials can convert electrical potential to mechanical motion, causing their dimensions to change with electrical potential or vice-versa. The force sensor measures the force between the AFM tip and the surface. When the tip moves across the surface, the control electronics receive the signals from the force sensors and use it to drive the piezoelectrics in order to maintain a constant probe-sample distance (Figure 41).

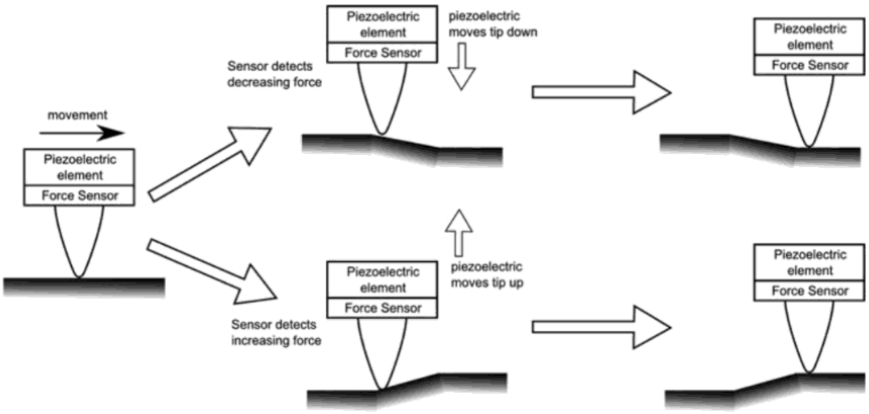

Figure 41 Feedback control

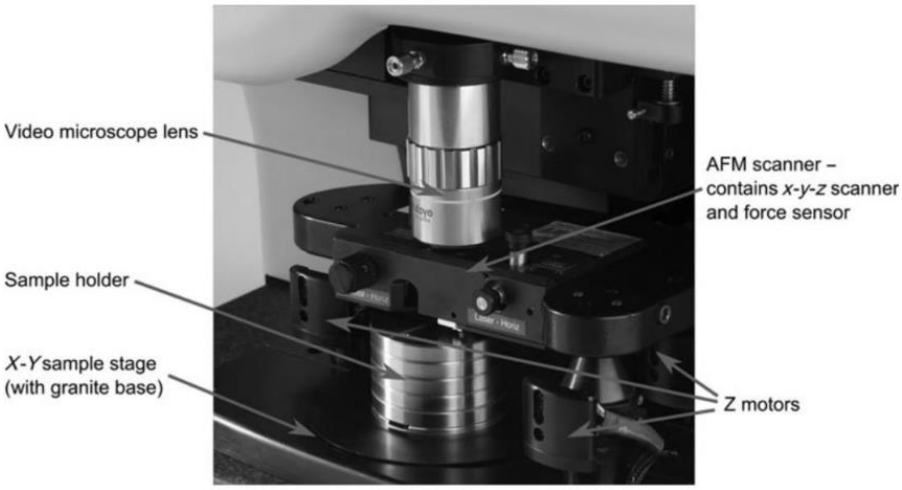

Figure 42 AFM stage and its components

Electrocatalytic H_2 production by LrGO

After irradiating the GO films and characterizing them, we chose the 'best 200nm thickness samples' irradiated with 170fs and 1ns pulse duration considering their sheet resistance and optical transmittance. A set of 3 LrGO films (different number of pulses per spot) for the two pulse durations, was given to collaborators from our laboratory to examine the electrocatalytic H_2 production by LrGO. In addition, a non-reduced GO film was given for comparison.

Then, the samples were used for the electrocatalysis as it is shown in the Figure below. An additional set of samples were coated with molecular catalysts for comparison.

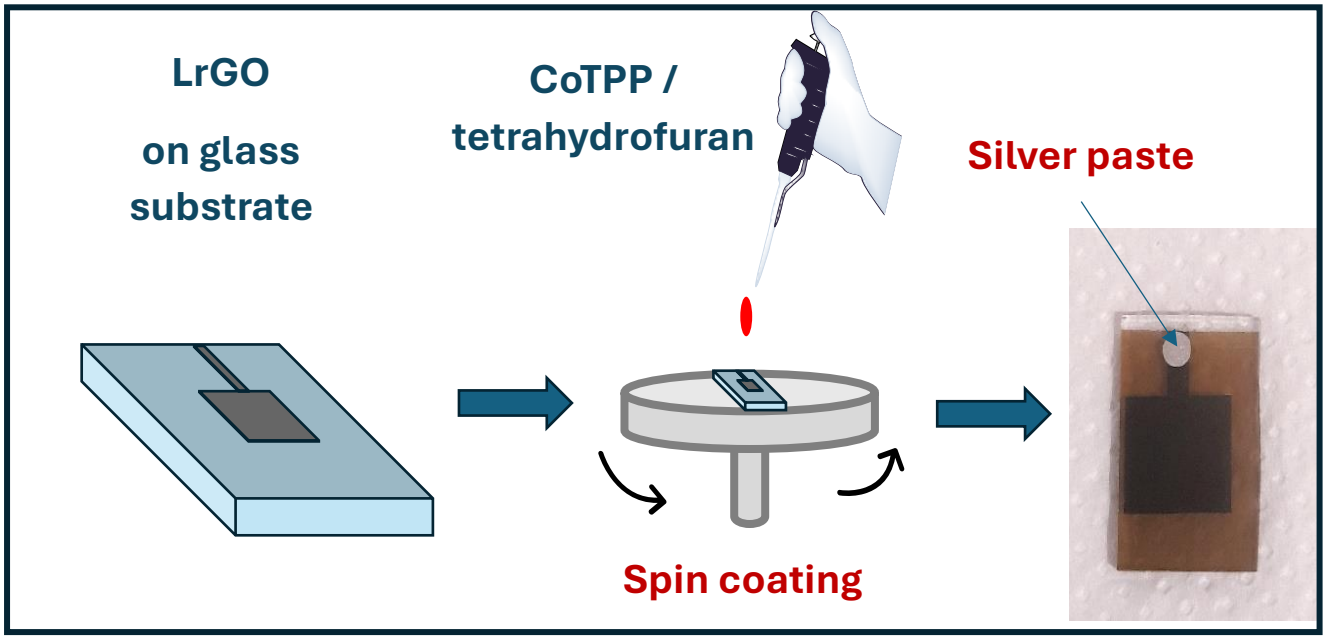

Figure 43 Functionalization with molecular catalysts

Figure 44 Electrocatalysis for H_2 production setup

We can express the electrocatalysis activity with quantities like overpotential (η), Tafel slope, current density, Onset potential and stability [42]. The Tafel slope and exchange current are two parameters to assess the activity expressed from the equation η =a+b logJ, where j is the current density, b is the Tafel slope and a is the exchange current density J_0 at zero overpotential.

Overpotential is the excess potential we need to break the thermodynamic potential at1.23V

Smaller Tafel slope means that we have greater density increment as a function of the overpotential change, thus faster electrocatalytic kinetics. A higher exchange current density means a greater charge transfer rate at a lower reaction barrier, as it describes the intrinsic charge transfer under equilibrium conditions.

For stability measurements, one method is the chronopotentiometry (E-t plot) where the longer the current density remains constant for a fixed potential. The longer it remains constant, the better the stability of the catalyst.

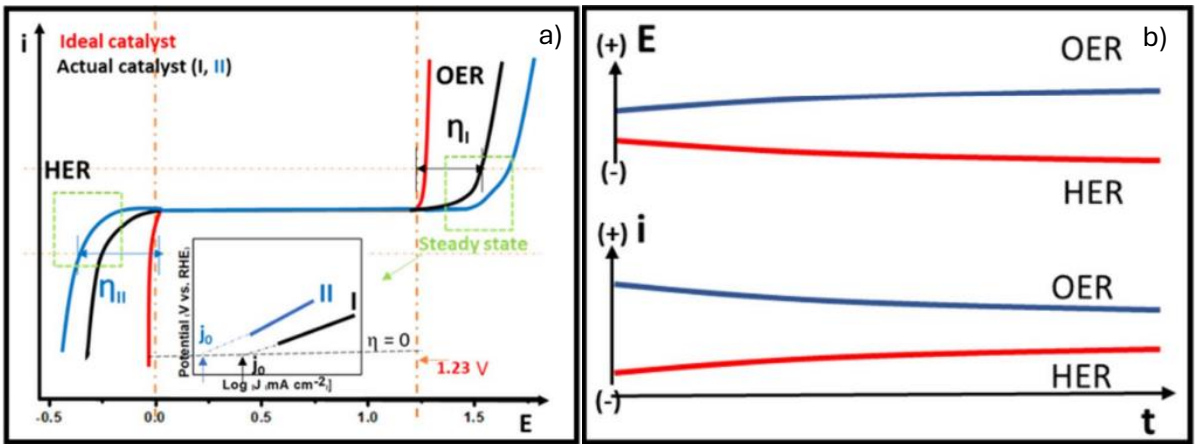

Figure 45 a) Activity in terms of overpotential, Tafel slope and exchange current density b) Stability in terms of current and potential-time curves[43]

Chapter 3: Results and Discussion

The irradiation was performed in air environment. The GO film surface was normal to the incident beam. The experiments were conducted in a wide range of energy fluences and pulses per spot, so that the optimal irradiation conditions for the GO reduction are found. After laser irradiation, the produced rGO films are first characterized by UV-Vis transmission and sheet Resistance measurements. These measurements are parametrized for three pulse durations (1ns, 150ps, 170fs) and two thicknesses (200nm, 100nm).

200nm GO film

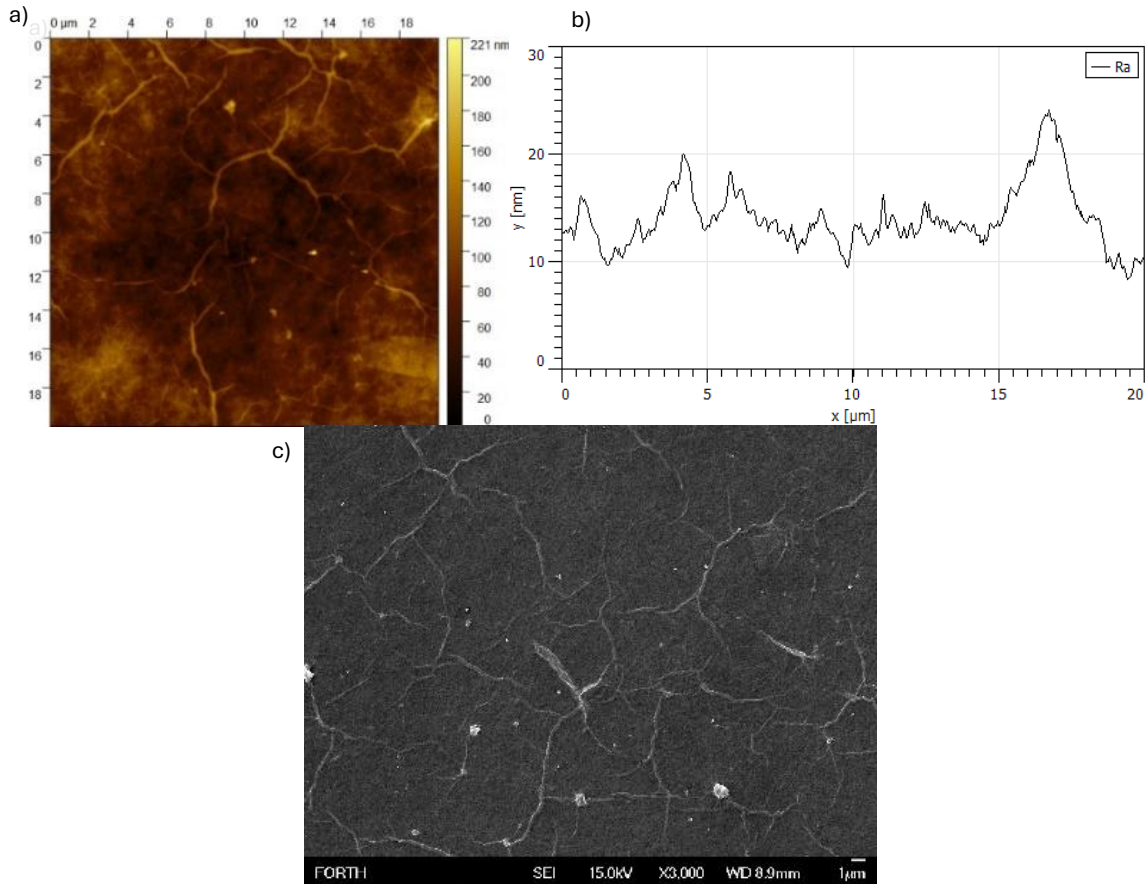

Figure 46 a) AFM of 200nm GO film, b) Roughness of the surface, c) SEM image of 200nm GO film

The AFM image of 200nm pristine GO film is illustrated above. Average roughness of Ra=(19,4±2,9)nm is obtained. The SEM image shows a uniform GO film.

A color map is plotted for each rGO film illustrating its transmittance and resistivity. For the Figures below, each point on the color map represents different values of fluence or pulses per spot. The color of each point corresponds to its value (sheet resistance or transmittance at λ=500nm) as indicated by the color scale bar.

The summarized color maps are plotted below:

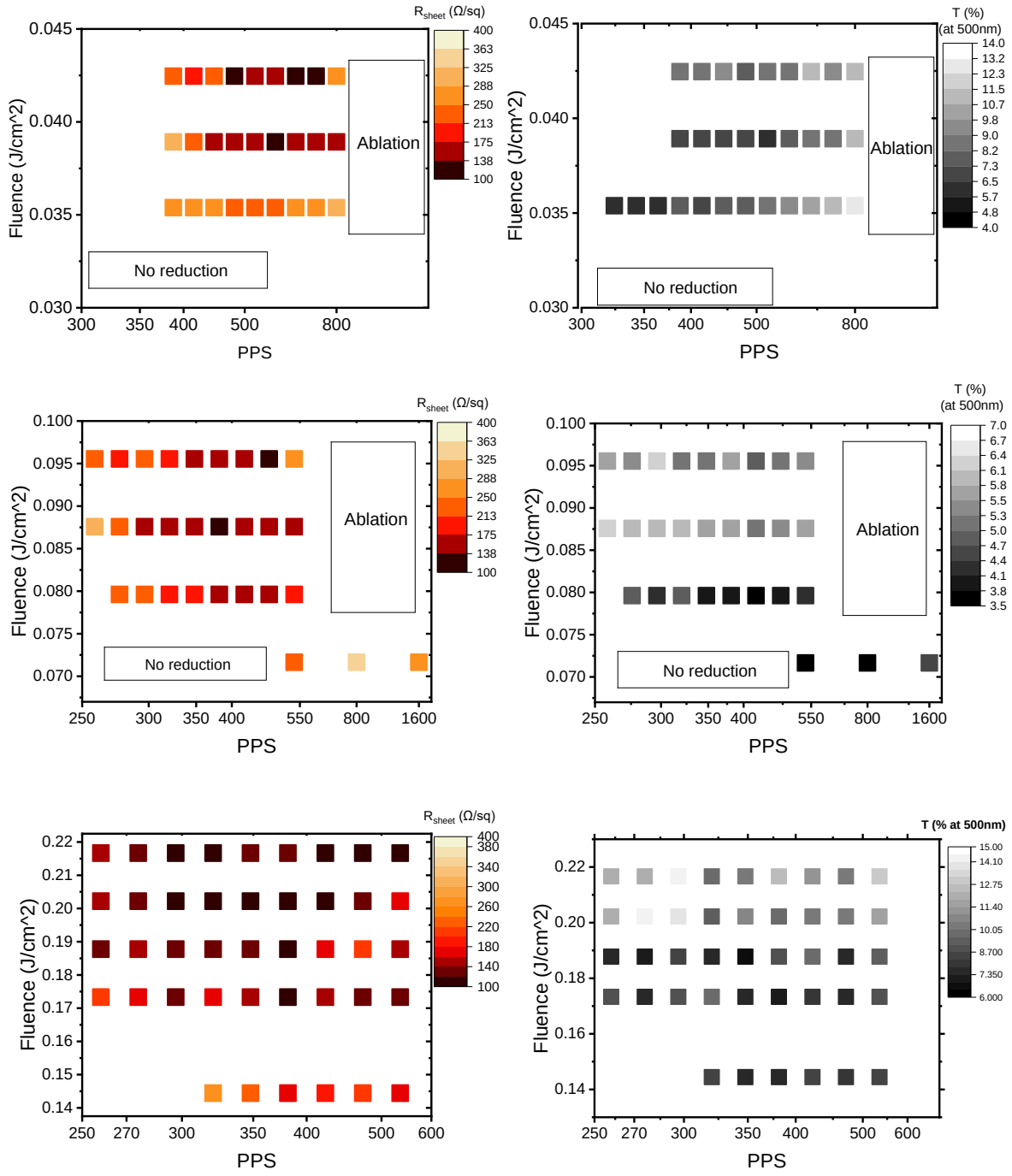

Figure 47 Color maps for 170fs, 150ps, 1ns (top to bottom) for Sheet resistance (right) and Transmittance (left)

From the Figures above, we can observe that for the 1ns pulse duration, there is a larger range of fluence and PPS that result to similar values of sheet resistance or transparencies. This range is much narrow in the fs and ps regime.

170fs pulse duration

Irradiating the GO film with 1026nm 170fs pulses, we need fluences above F=0.035 J/cm^2. Irradiating with lower fluences results in no reduction on the sample. In addition, for a low number of pulses per spot (PPS) (high scanning speed on XY stages) results in no reduction. Increasing the number of pulses submerges an extreme reduction of its sheet resistance. Further increase of irradiation results in film ablation, which subsequently increases its sheet resistance.

Similar behavior is observed from the transmittance spectra. Upon irradiation, the GO film turns from a yellow-brown color to dark brown/black when reduced. This is observed from the transmittance spectra above. For ~350 PPS or more, reduction occurs, and the film becomes less transparent. Further increasing the PPS, the film is ablated and becomes more transparent.

During this study we tried to define the best rGO conditions considering the potential of these layers to be used as i) transparent electrodes and ii) in electrocatalysis. For electrocatalysis we try to achieve the highest possible conductivity, while for transparent electrodes we should find the optimal conditions for a balanced combination between high conductivity and high transparency. Nevertheless, in this thesis only results of rGO in electrocatalytic H_2 production are shown.

More detailed plots are presented below, with exact values of Sheet resistances and transmittance:

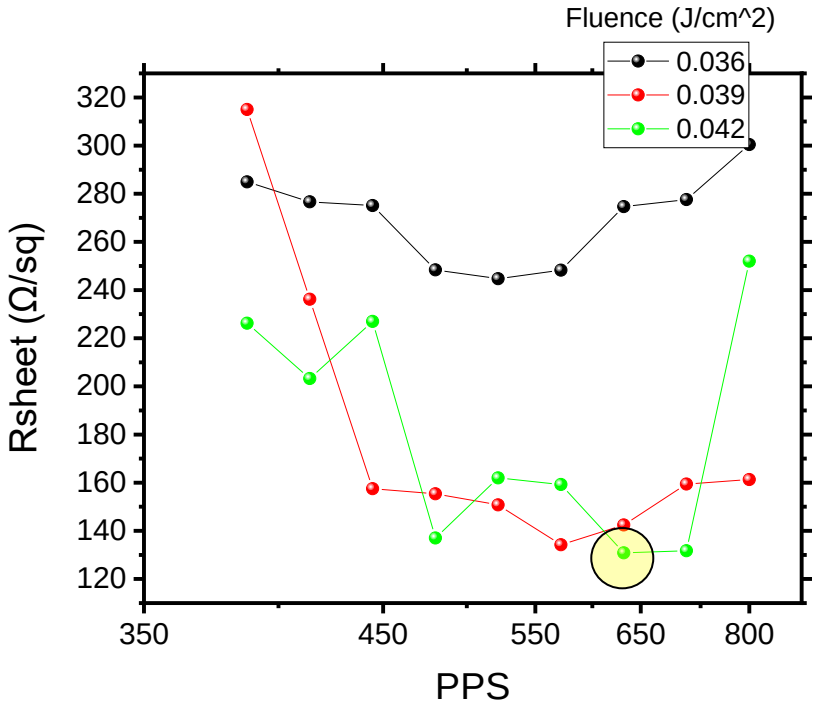

Figure 48 Sheet resistance as function of PPS for 170fs pulses

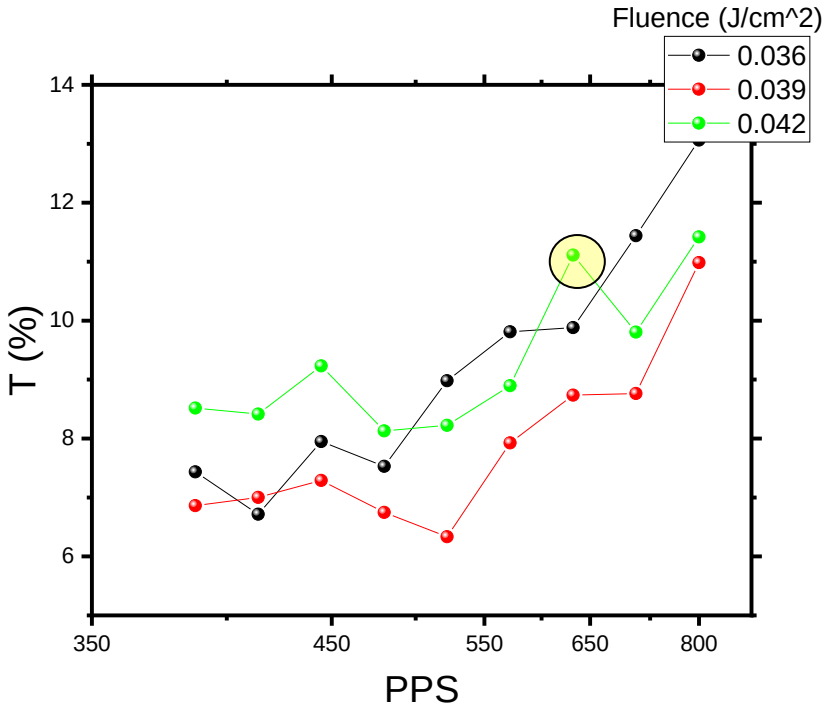

Figure 49 Transmittance as a function of PPS for 170 fs pulses

From both sheet resistance and transmittance spectra, we can notice that while increasing the PPS, both Sheet resistance and transmittance decreases at first, and then increases again. The best conditions compromising sheet resistance for good transmittance is irradiating the GO film with **F=0.042J/cm^2 and 631PPS.**

150ps pulse duration

Likewise, the Figures for 150ps pulses are presented below:

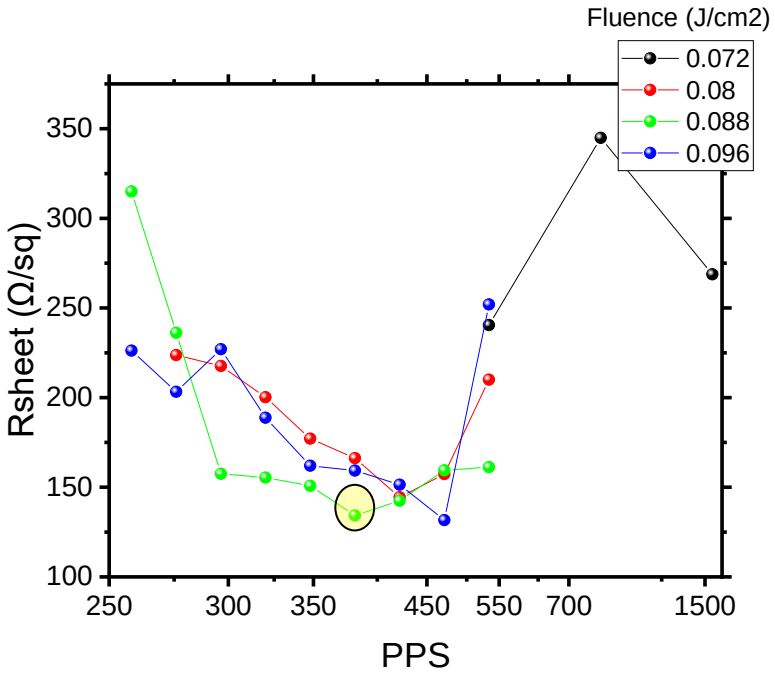

Figure 50 Sheet resistance as a function of PPS for 150ps pulses

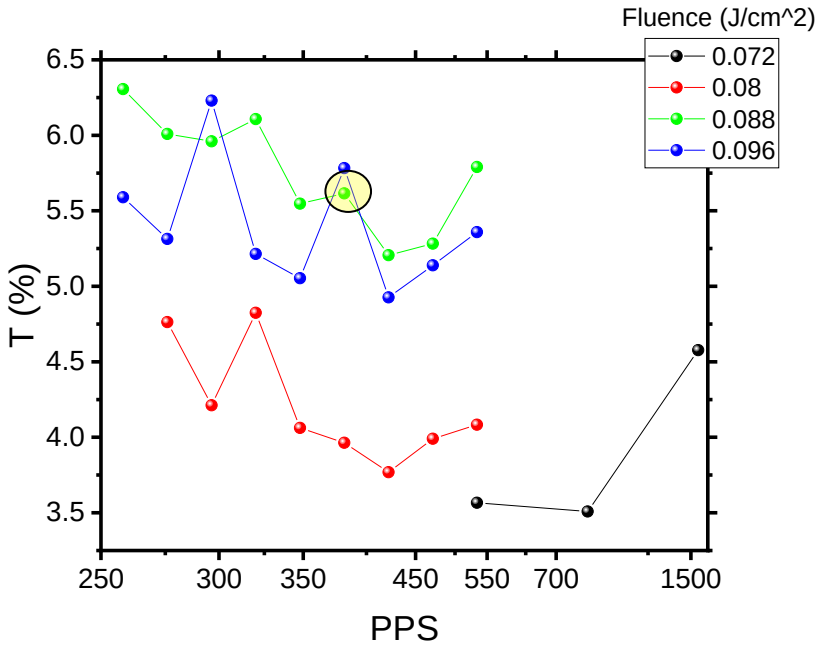

Figure 51 Transmittance as a function of PPS for 150ps pulses

We observe that compared to the 170fs pulses, we need higher fluencies to achieve reduction, but less PPS. Sheet resistances are not much deviated; however, the transparency is reduced. The best conditions compromising sheet resistance for good transmittance is irradiating the GO film with **F=0.088J/cm^2 and 380PPS.**

1ns pulse duration

Continuing, the plots for 1ns pulse duration irradiation is presented below:

From Figure 47, the first observation is that for nanosecond pulses, there is a wider range of laser fluences and number of pulses that results in similar sheet resistances and transmittance. Secondly, the fluences required to reduce the GO films are further increased compared to ps and fs pulse durations.

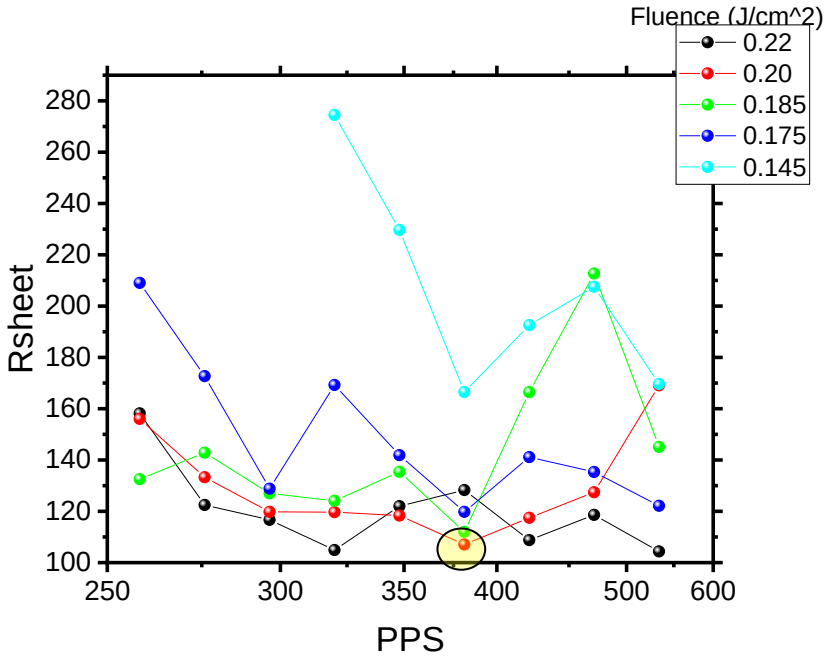

Figure 52 Sheet resistance as a function of PPS for 1ns pulses

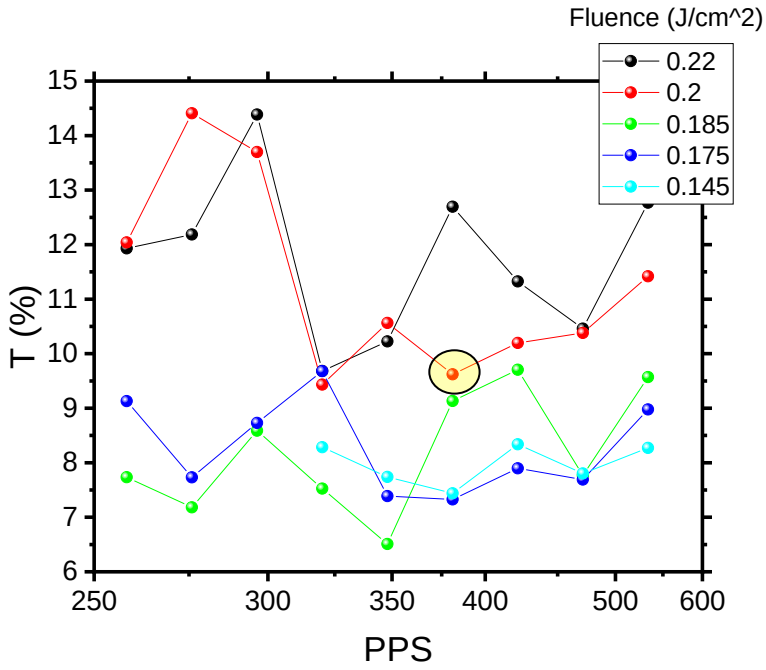

Figure 53 Transmittance as a function of PPS for 1ns pulses

The best conditions compromising sheet resistance for good transmittance is irradiating the GO film with **F=0.20J/cm^2 and 380PPS.**

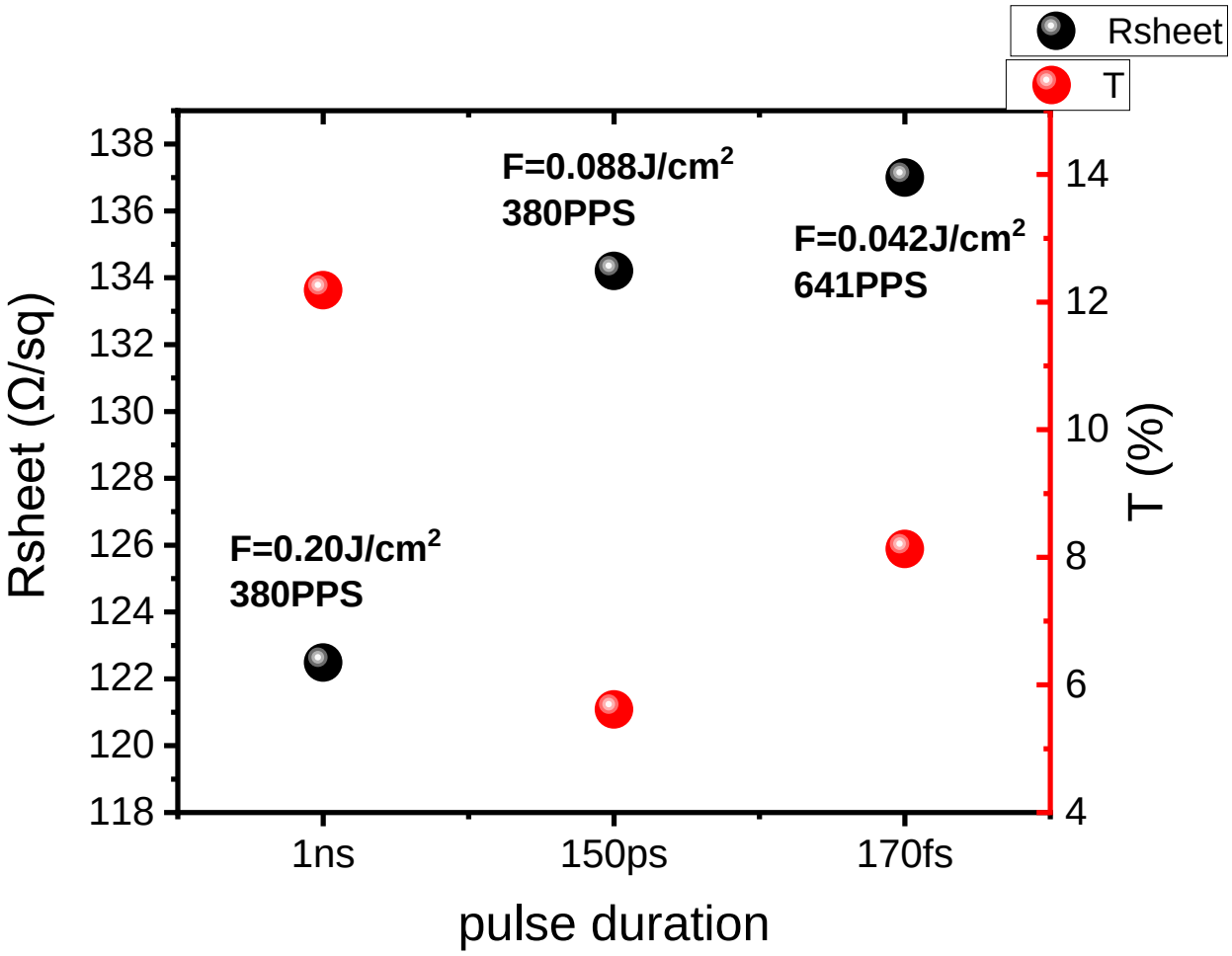

Figure 54 Comparison of best rGO samples per pulse duration (200nm thickness)

In the Figure above, the best results per pulse duration are plotted. We can notice that for shorter pulse durations, we need less energy fluence to induce reduction on the GO film. This phenomenon agrees with [44]. Two photon absorption may occur and induce photochemical removal of some carbonyl groups and hydroxy groups. Nevertheless, similar results are obtained comparing the irradiation with the 3 different pulse durations. A spectacular decrease in Sheet resistance (pristine GO film has R_{sheet}=9.87x10^{8}Ω/sq) is observed.

100nm GO film

The next step is repeating the same process for the thinner 100nm GO film. Similarly, the color maps are presented below:

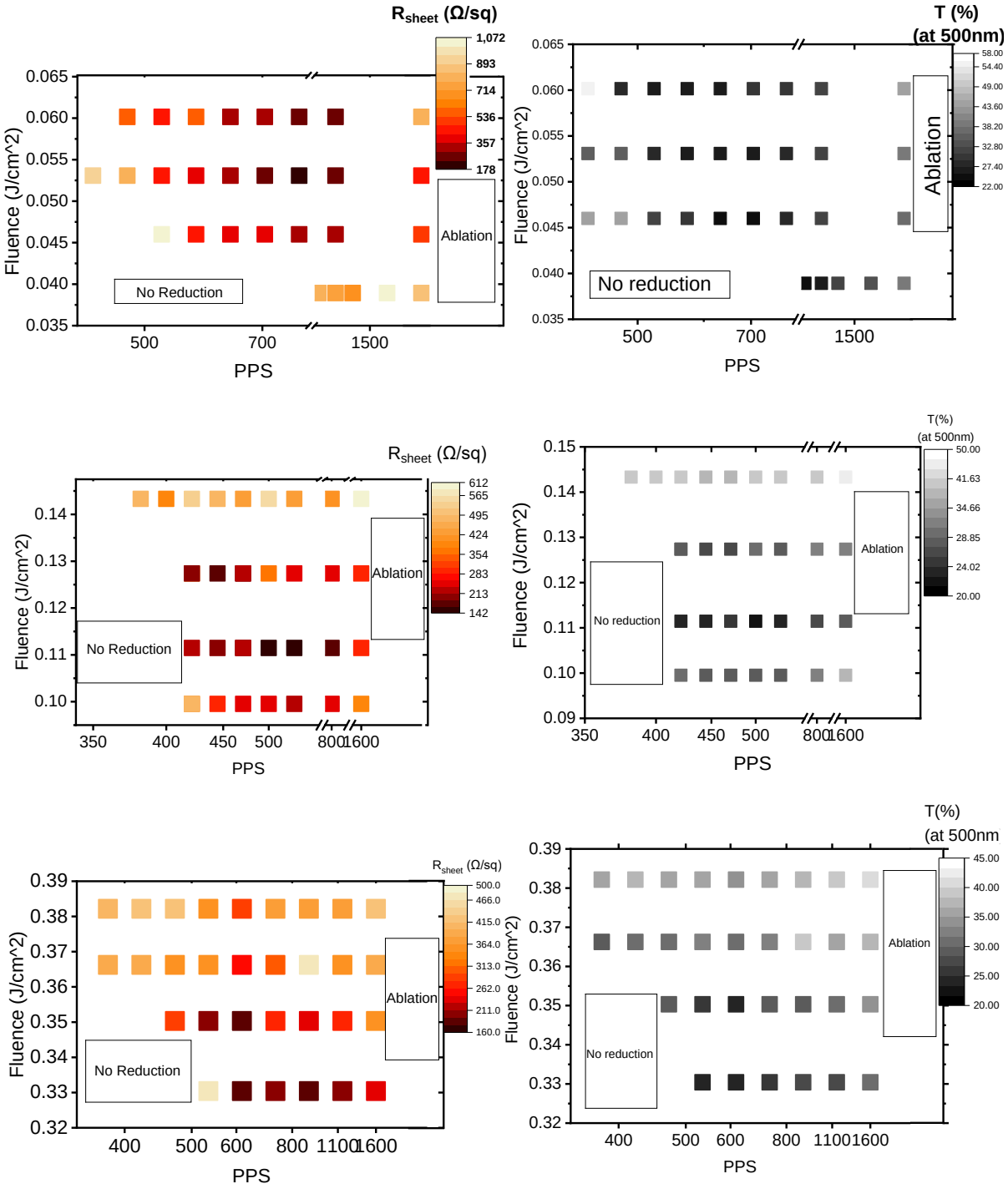

Figure 55 Color maps for 170fs, 150ps, 1ns (top to bottom) for Sheet resistance (right) and Transmittance (left)

170fs pulse duration

We can see that the reduction of 100nm GO films follows the same trend as the thicker 200nm films. It is evident that for the thinner film, more energy fluence and more PPS are required to properly reduce the GO film. In addition, there is more deviation between the samples with different irradiating conditions compared to the thicker film. The exact reason that more energy is required in thinner films is not absolutely clear.

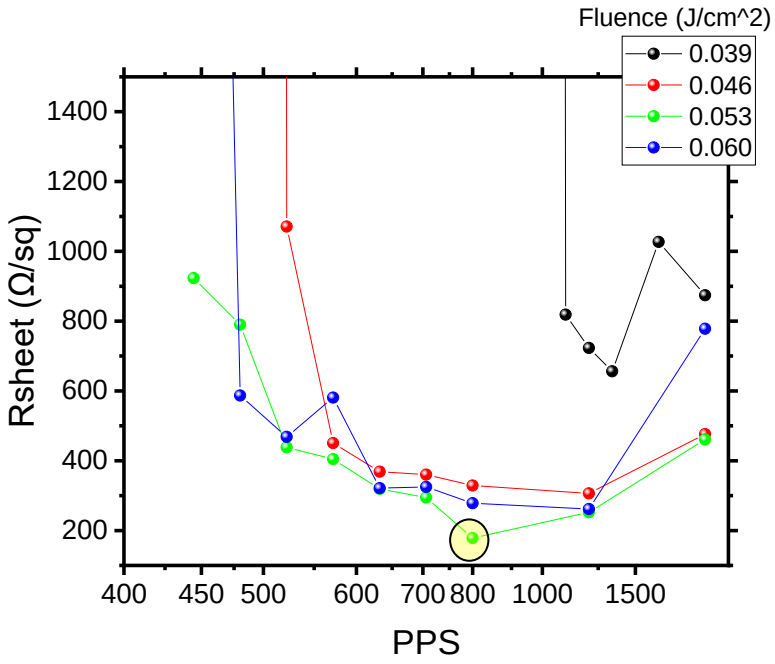

Figure 56 Sheet resistance as a function of PPS for 170fs pulses

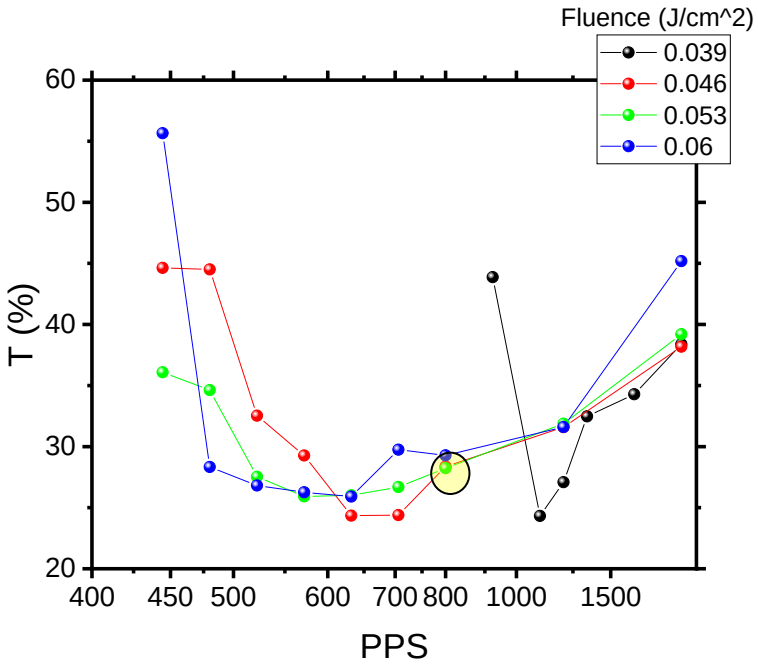

Figure 57 Transmittance as a function of PPS for 170fs pulses

The best conditions compromising sheet resistance for good transmittance is irradiating the GO film with **F=0.053J/cm^2 and 800PPS.**

150ps pulse duration

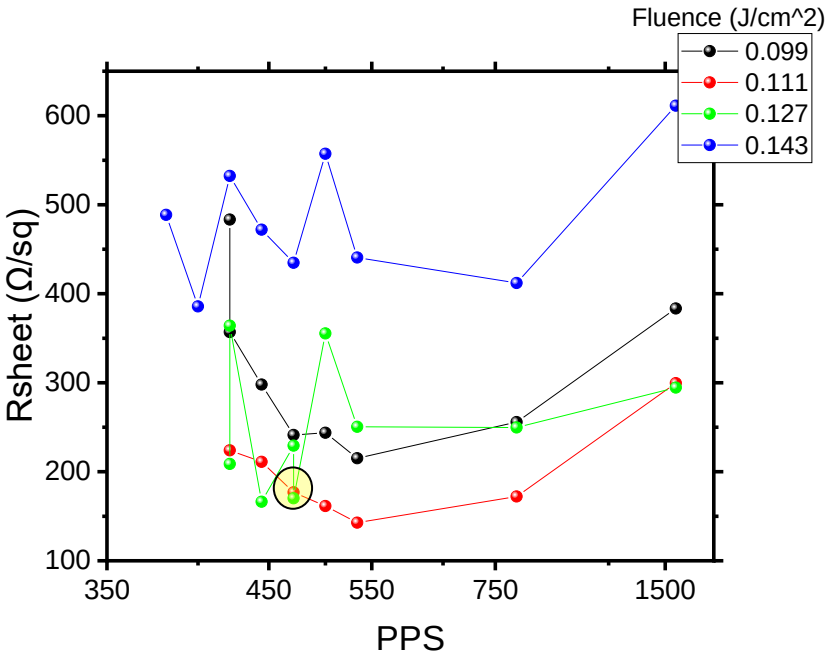

Figure 58 Sheet Resistance as a function of PPS for 150ps pulses

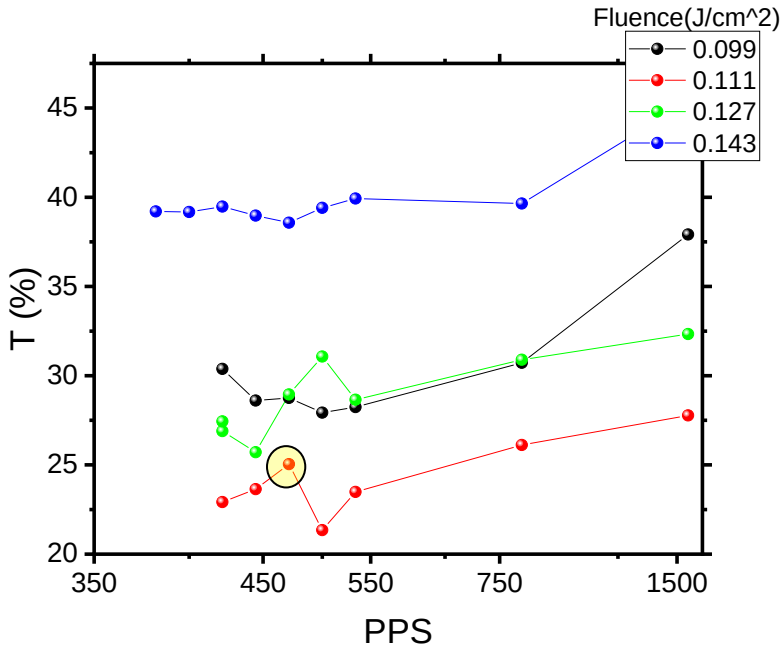

Figure 59 Transmittance as a function of PPS for 150ps pulses

Likewise, the best conditions compromising sheet resistance for good transmittance is irradiating the GO film with **F=0.111J/cm^2 and 470PPS.**

1ns pulse duration

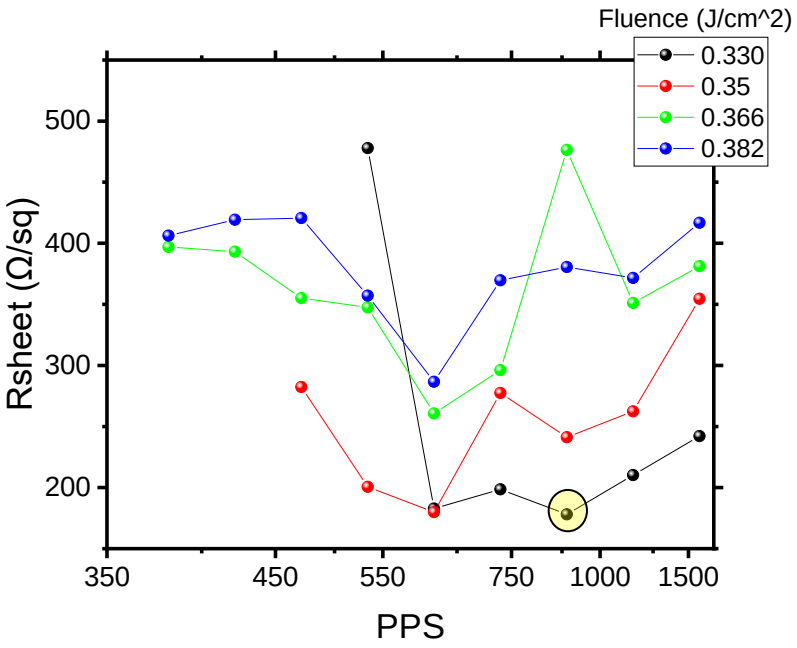

Figure 60 Sheet resistance as a function of PPS for 1ns pulses

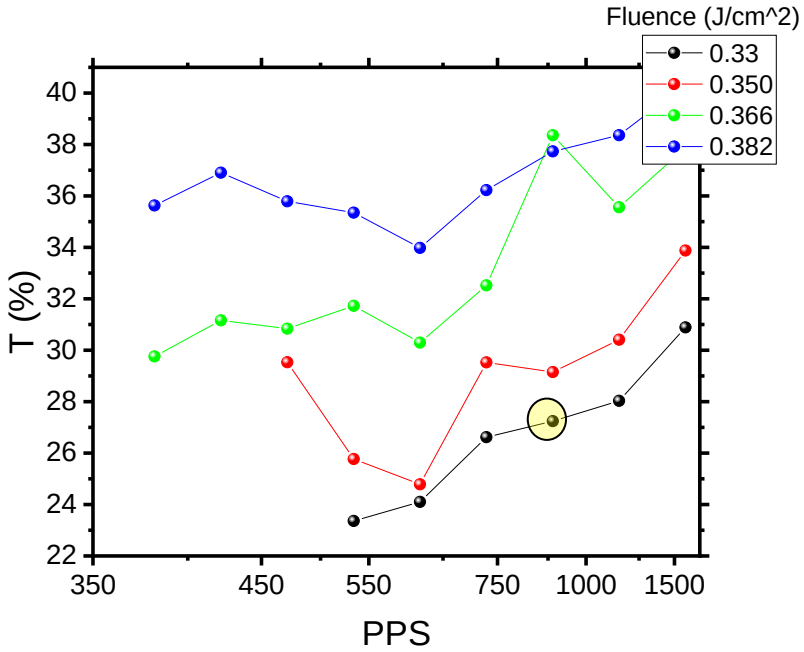

Figure 61Transmittance as a function of PPS for 1ns pulses

Lastly, for the 1ns pulse duration, 100nm thickness, the best conditions are **F=0.330J/cm^2 and 888PPS**.

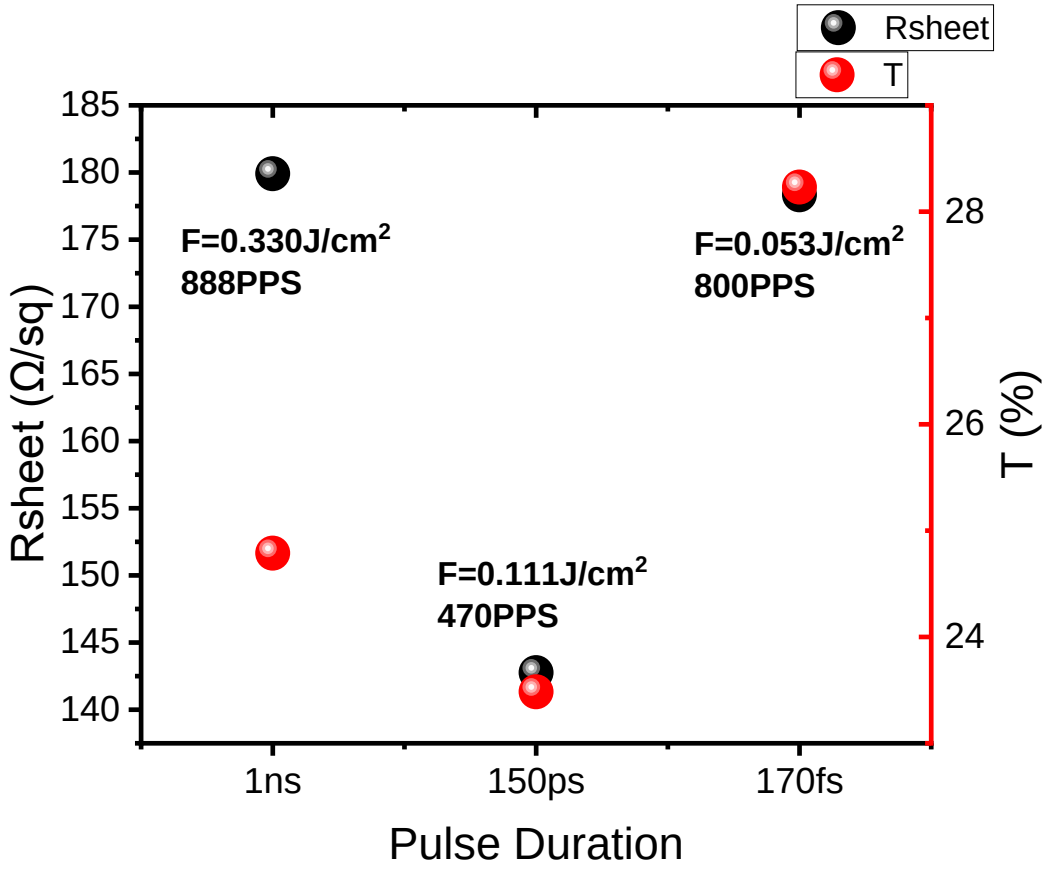

Figure 62 Comparison of best rGO samples per pulse duration (100nm thickness)

In the Figure above, the best results per pulse duration are plotted. We can notice that for shorter pulse durations, we need less energy fluence to induce reduction on the GO film as for the 200nm film thickness. Moreover, larger fluences and more PPS are needed, compared to the 200nm best conditions for each pulse duration. In addition, compared to the 200nm film, we achieve higher transparencies, in the expense of higher sheet resistance. A general conclusion of the above study regarding the application of GO in solar cells and transparent electrode could be the following. If we need conductive transparent electrodes, we can deposit thinner films and achieve higher transparencies, but expect higher resistances.

Raman spectra:

We perform Raman analysis in some of the 200nm rGO layers. In particular, as we would like to study the impact of the reduction level on the Raman spectra, we choose to analyze the points highlighted with yellow in Figure 63 and 63. That means we choose three different conditions corresponding to i) partly reduced GO, ii) well reduced and iii) post-reduction, which means that the material is reduced and partly ablated. These conditions are shown below:

170fs pulse duration

Figures 63 and 64 are the same as Figures 48 and 49 respectively. The three conditions mentioned above are highlighted and mentioned in table 2.

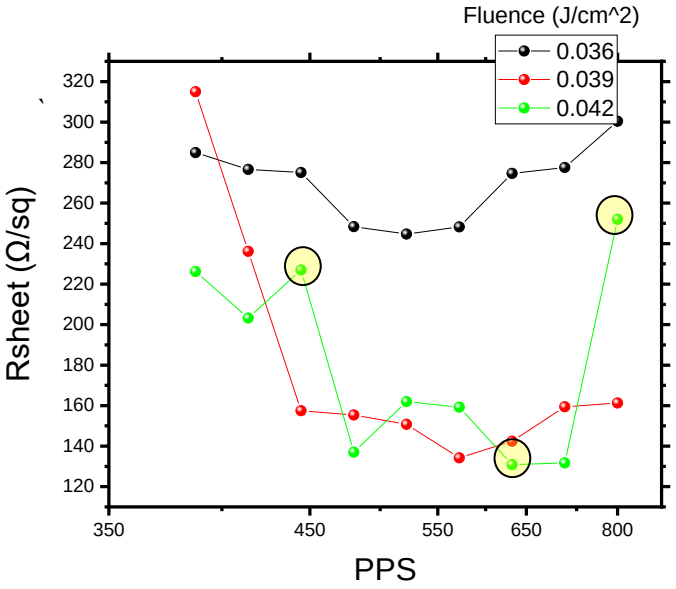

Figure 63 Sheet resistance as a function of PPS for 170fs pulses

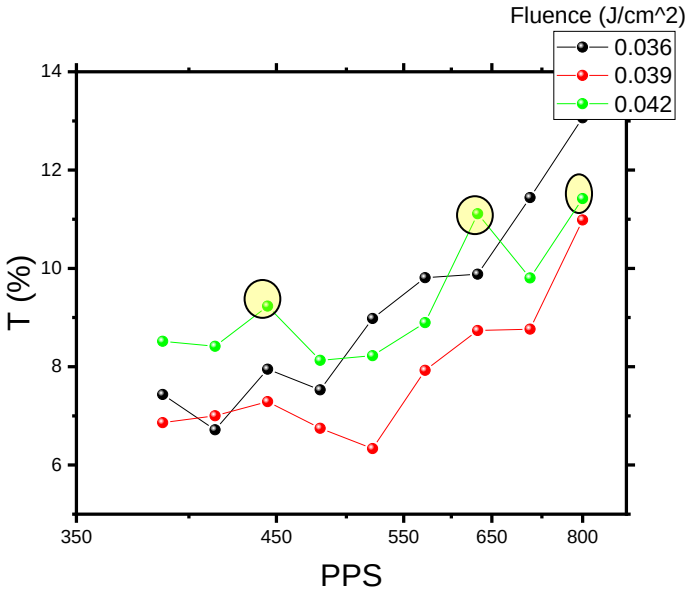

Figure 64 Transmittance as a function of PPS for 170fs pulses

Before	Best	After	Pristine GO
F=0.042J/cm^2, 444PPS R_{sheet}=227Ω/sq T=9.2%	F=0.042J/cm^2, 631PPS R_{sheet}=130Ω/sq T=11%	F=0.042J/cm^2, 800PPS R_{sheet}=252Ω/sq T=11.4%	R_{sheet}=9.87x10^{8}Ω/sq T=39.4%

Table 2 Parameters for 170fs pulse duration

1ns pulse duration

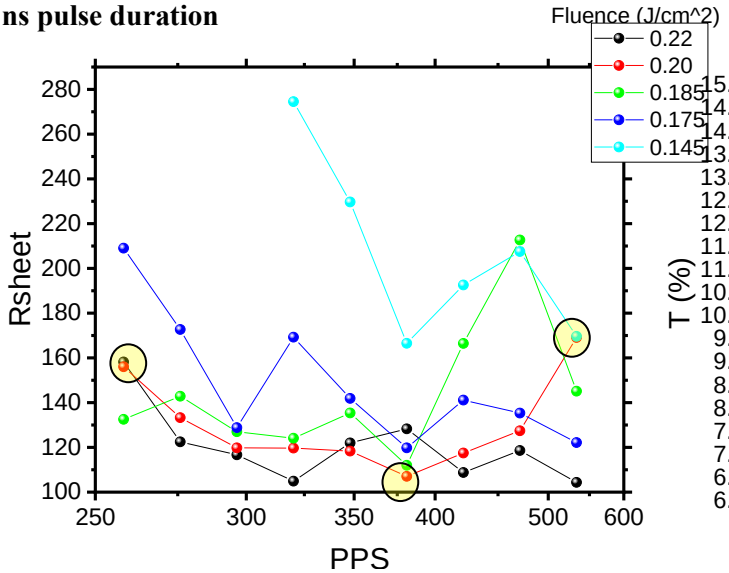

Figure 65 Sheet resistance as a function of PPS for 1ns pulses

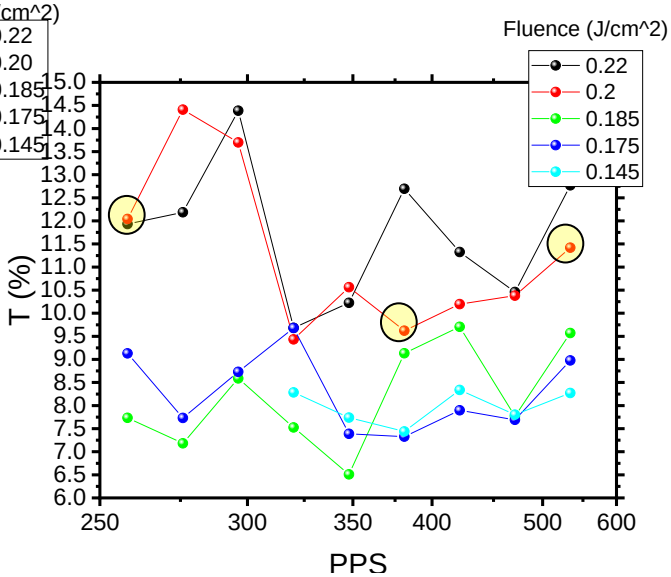

Figure 66 Transmittance as a function of PPS for 1ns pulses

Before	Best	After
F=0.20J/cm^2, 258PPS 156Ω/sq T=12%	F=0.20J/cm^2, 380PPS 107Ω/sq T=9.6%	F=0.20J/cm^2, 533PPS 169Ω/sq T=11.4%

Table 3 Parameters for 1ns pulse duration

Likewise, the Figures 65 and 66 are the same as 52 and 53 respectively, with the 3 conditions discussed highlighted and summarized in the table above.

The Raman spectra for the **170fs** pulse duration sample set is shown below:

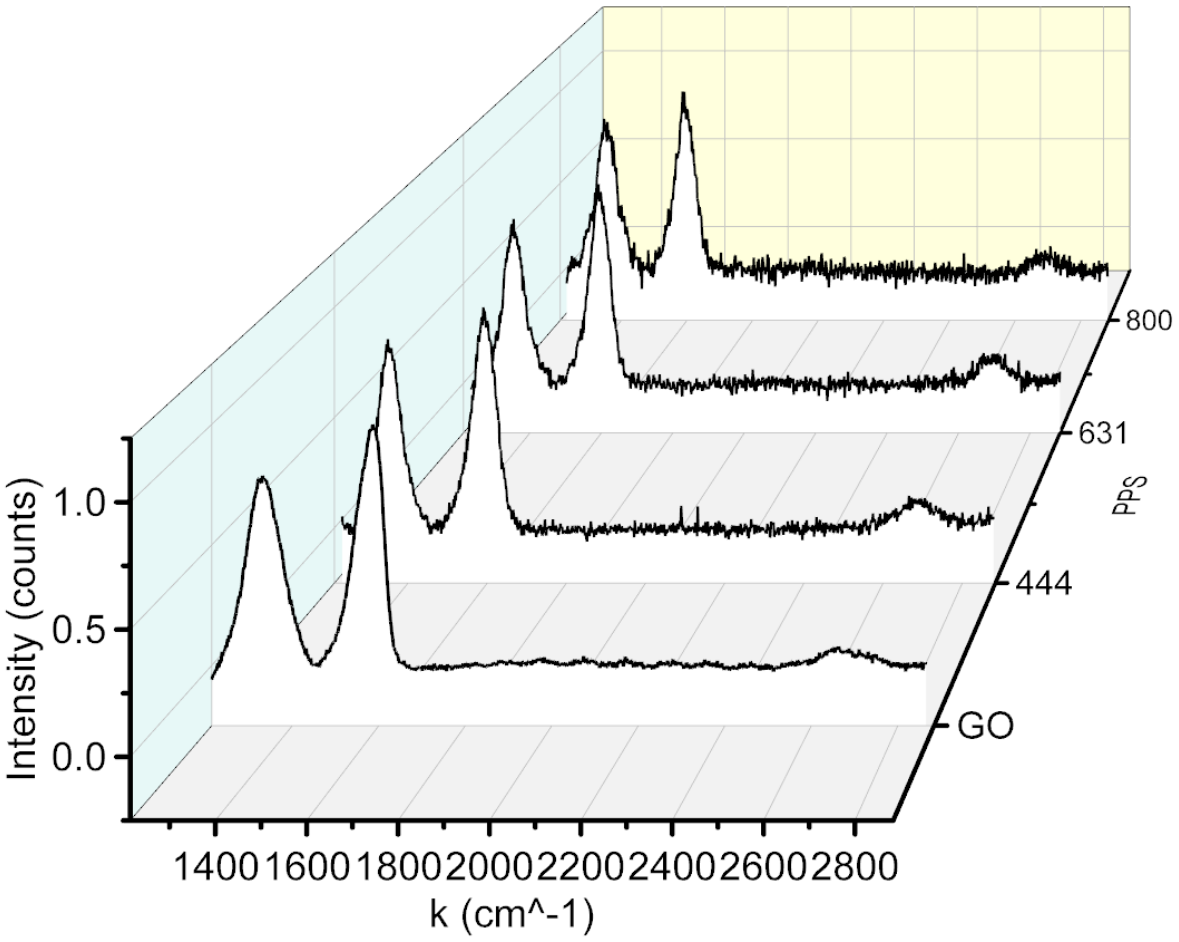

Figure 67 Raman spectra for 170fs pulse duration

All plots are normalized to the G band. For pristine GO the D and G bands are at k=1330cm^{-1} and k=1586cm^{-1} respectively. The 2D band is weak as expected. Upon irradiation, both bands are shifted towards longer wavenumbers. The ratio of I_D to I_G intensity is a measure of the lattice disorder as previously mentioned. Additionally, the ratio of I_{2D} to I_G intensity is a measure of conversion to graphene-like structure[17]. Ratios are shown in the Figure below:

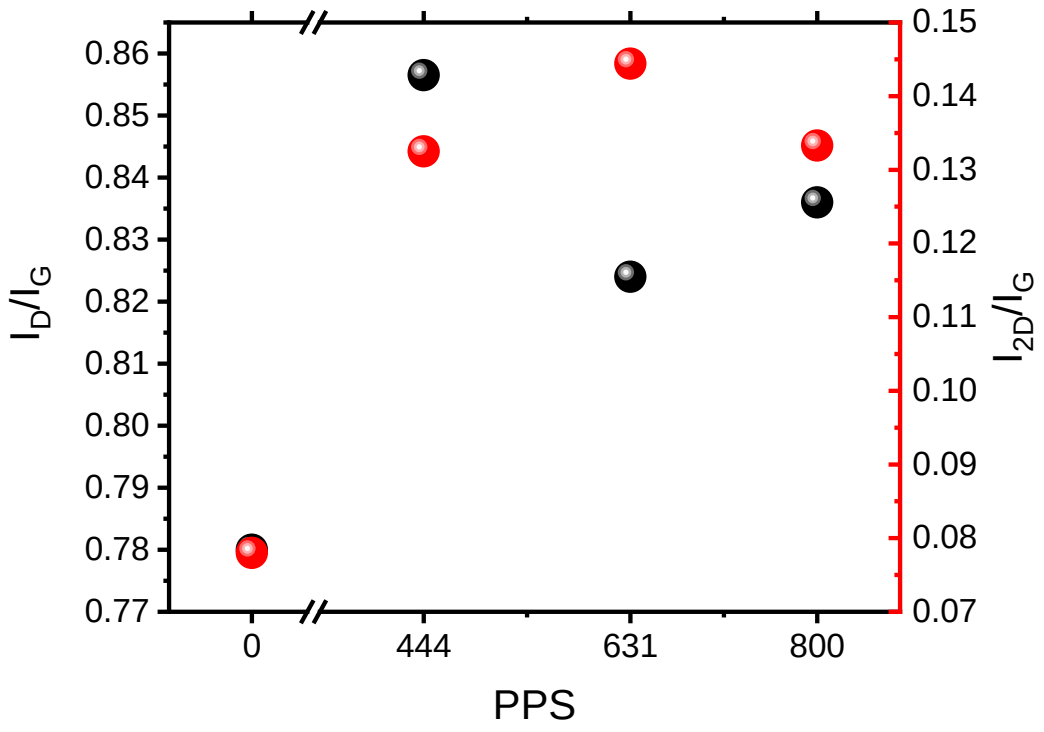

Figure 68 I_D/I_G(black), I_{2D}/I_G(red) intensity ratios for 170fs pulses

For pristine GO film, both I_D/I_G and I_{2D}/I_G ratios are low compared to the rGO films. Thus, by irradiating we introduce defects to the lattice. However, the graphene-like structure is restored, as the I_{2D}/I_G increases from 0.78 to ~0.85. The highest I_{2D}/I_G ratio and lowest I_D/I_G is found for the sample irradiated with 631PPS, confirming our previous assumption to label it as the best reduction (lowest sheet resistance).

In addition, we can see that increasing PPS from 444 to 631, I_D/I_G ratio tends to decrease, while increasing from 631 to 800 increases I_D/I_G ratio. This is in agreement with the findings of[31].

The Raman spectra for the **1ns** pulse duration sample set is shown below:

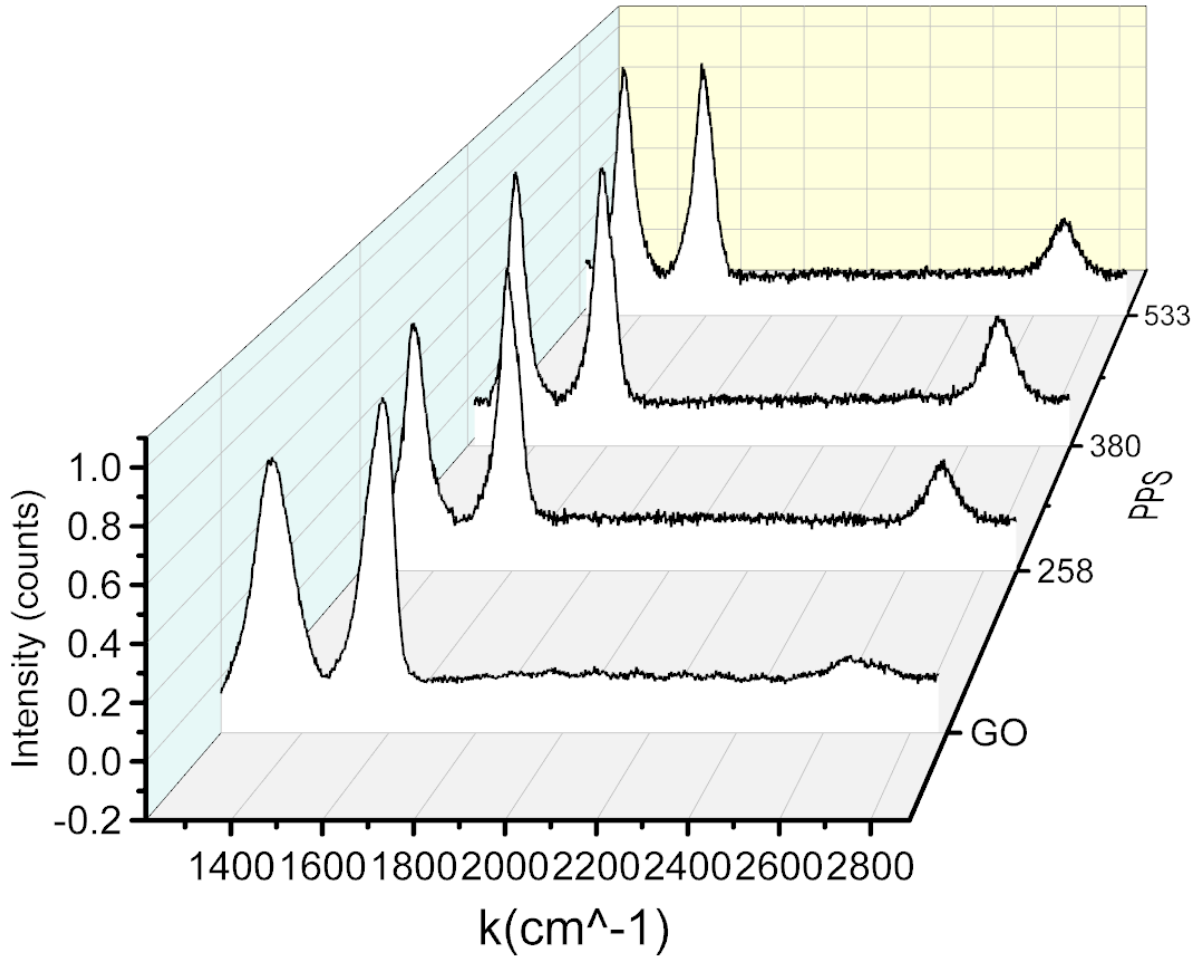

Figure 69 Raman spectra for 1ns pulse duration

Similar to the previous case, all plots are normalized to the G band. For pristine GO the D and G bands are at k=1330cm^{-1} and k=1586cm^{-1} respectively. Ratios are shown in the Figure below:

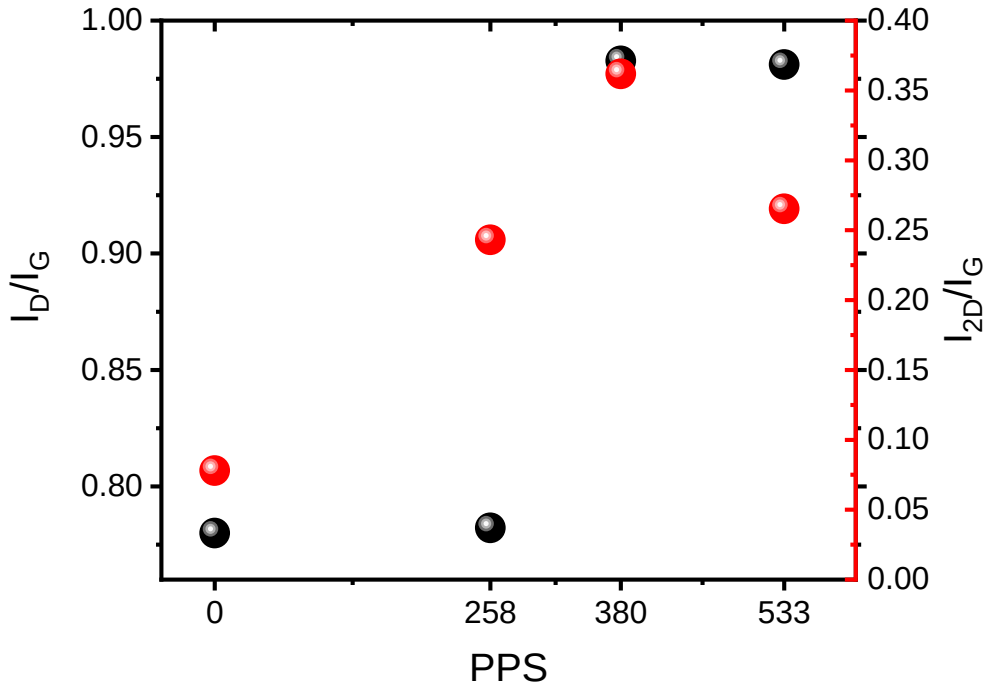

Figure 70 I_D/I_G(black), I_{2D}/I_G(red) intensity ratios for 1ns pulses

Likewise, the I_{2D}/I_G ratio is increased upon irradiation. However, the I_D/I_G ratio increases monotonically upon increasing the number of pulses. This confirms the findings of [31] as in nanosecond pulses, thermal effects are dominant, introducing defects in the lattice. In addition, both I_D/I_G and I_{2D}/I_G ratios are higher than the case of fs pulses.

According to Childres et al. [45] ,I_D/I_G ratio shows two different behaviors. At first, for low defect regime, the ration increases as defect density increases because the more the defect density the more elastic scattering is created. After a value of defect density, I_D/I_G ratio starts to decrease as a result of a more amorphous carbon structure, attenuating all Raman peaks. This behavior is shown in the Figure below. From our findings, we notice that 1ns is in the first regime, while 170fs pulses are in the second regime.

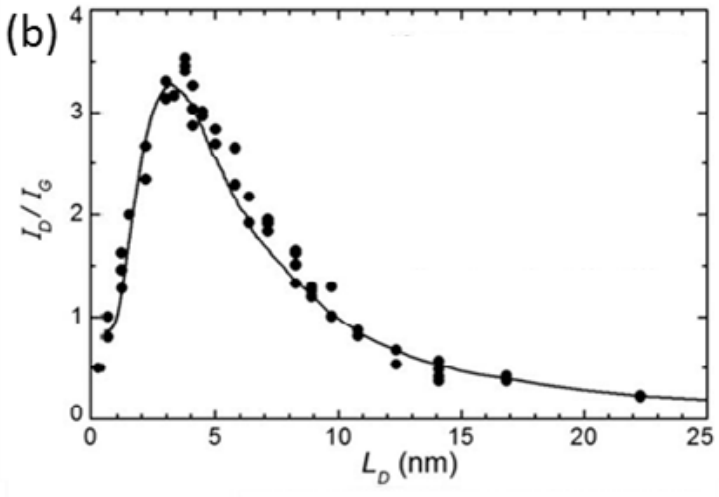

Figure 71 I_D/I_G ratio compared to the average defect distance[45]

Surface Morphology

To investigate the role of the surface morphology on the previous results, we study the surface morphology through SEM microscopy.

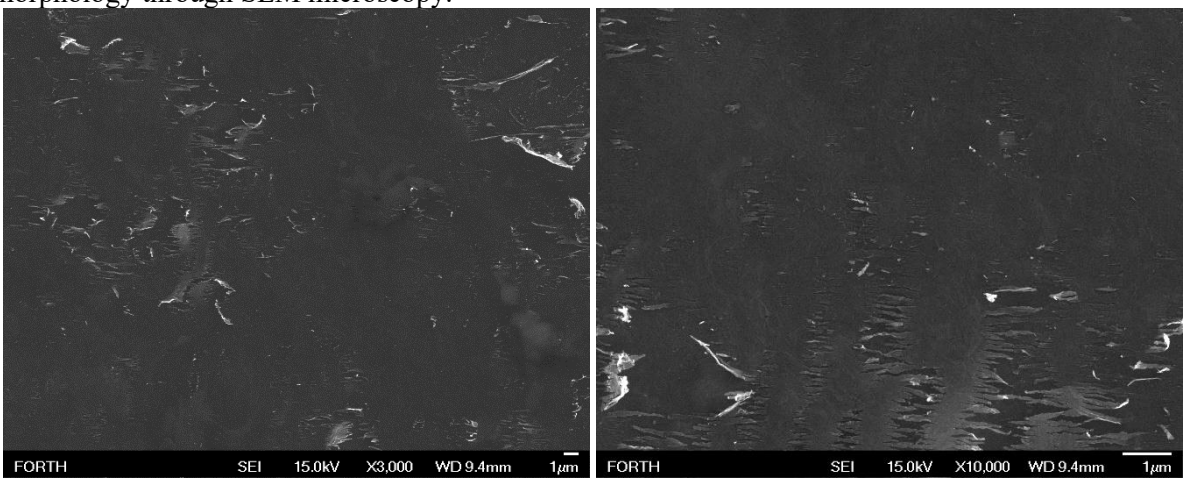

Figure 72 SEM images for 444PPS 170fs pulses (x3000,x10000 magnification)

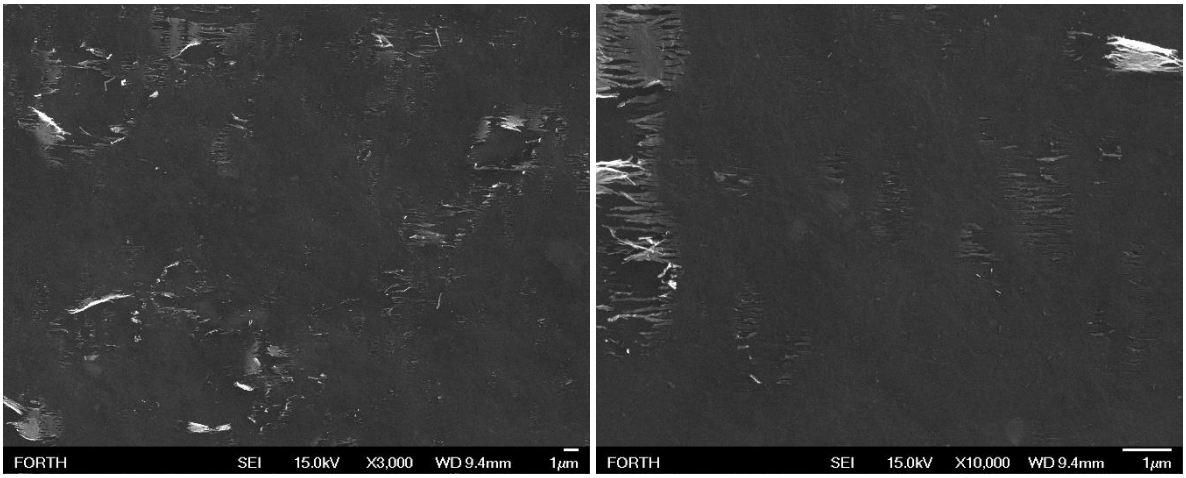

Figure 73 SEM images for 631PPS 170fs pulses (x3000,x10000 magnification)

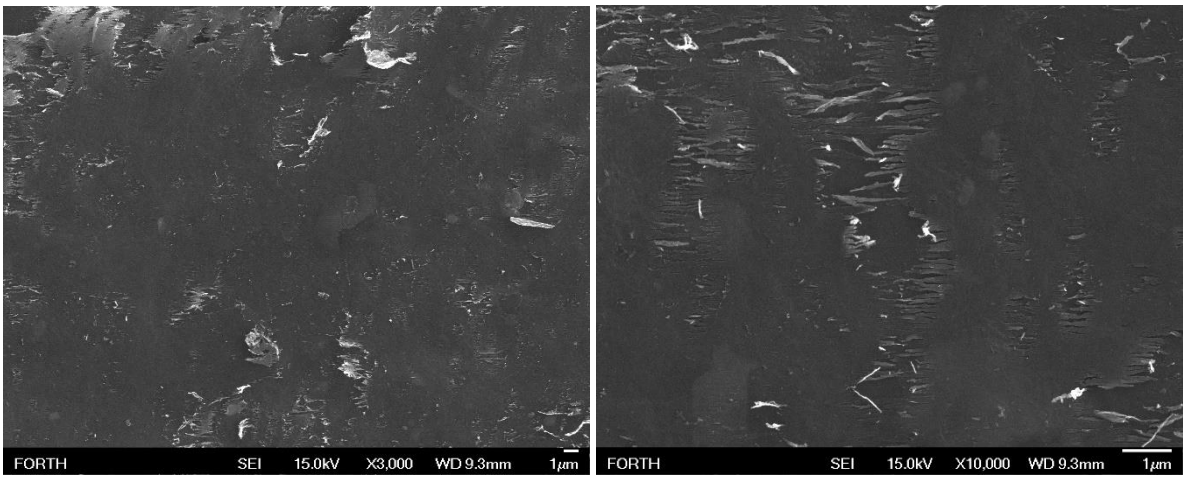

Figure 74 SEM images for 800 PPS 170fs pulses (x3000,x10000 magnification)

From the Figures above, we can see that while increasing the number of pulses per spot, we have intense defoliation of the graphene sheets.

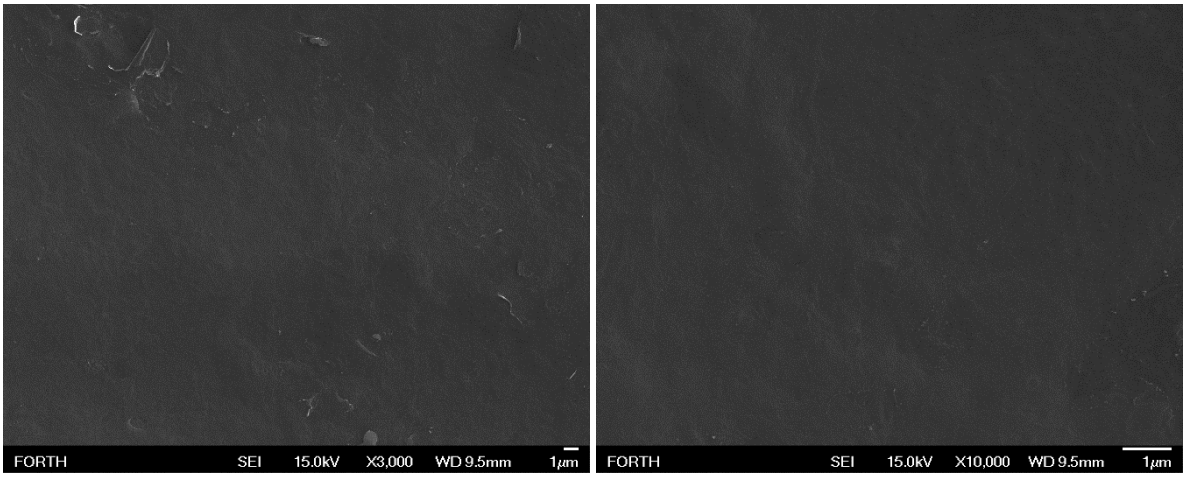

Figure 75 SEM images for 258 PPS 1ns pulses (x3000,x10000 magnification)

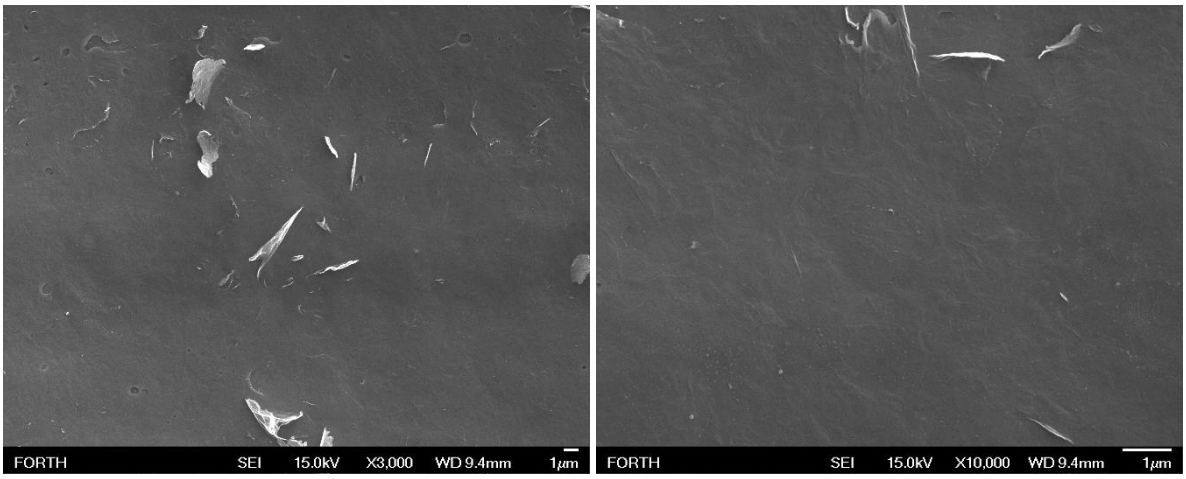

Figure 76 SEM images for 380 PPS 1ns pulses (x3000,x10000 magnification)

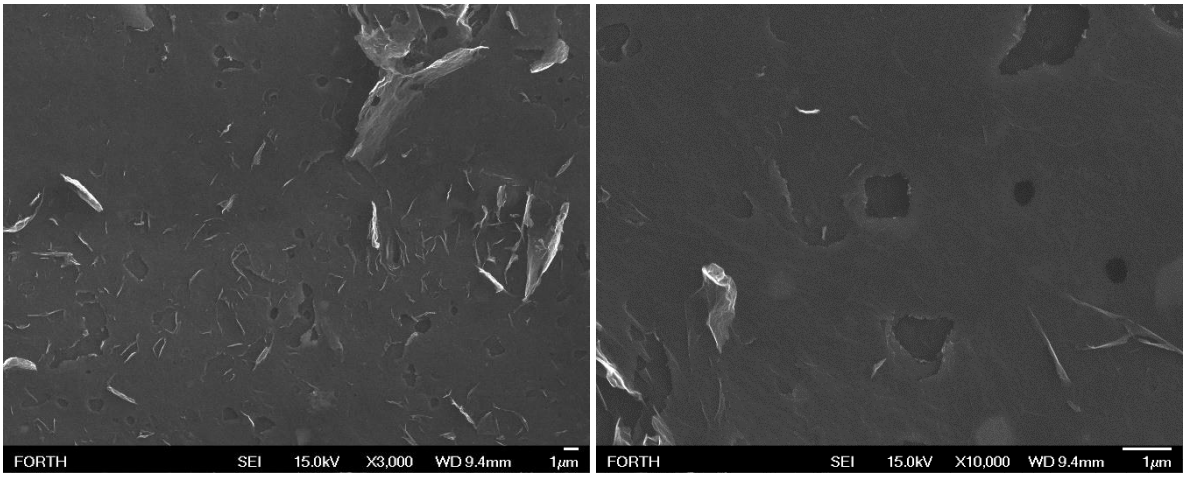

Figure 77 SEM images for 533 PPS 1ns pulses (x3000,x10000 magnification)

In the case of 1ns pulse duration, the film's quality is better, with less defoliation occurring. Still, for a high number of PPS, ablation of the surface is noticeable. It seems that the findings from the SEM analysis may explain the behavior of the I_D/I_G trend, as the ns laser-processed surface appears to contain a lower number of defects compared to fs.

GO and rGO in H_2 production

Nowadays, we notice the depletion of fossil fuels in the current world because of their importance as the primary source of energy for many countries. In addition, challenges such as global warming, the fluctuating prices of oil and the depletion of fossil fuels, forces us to make the transition from traditional non-renewable sources of energy to cleaner-green energy sources[46,47]. Sources like solar, wind, biomass and hydrogen energy have become topics of interest as they are green, environmentally friendly sources.

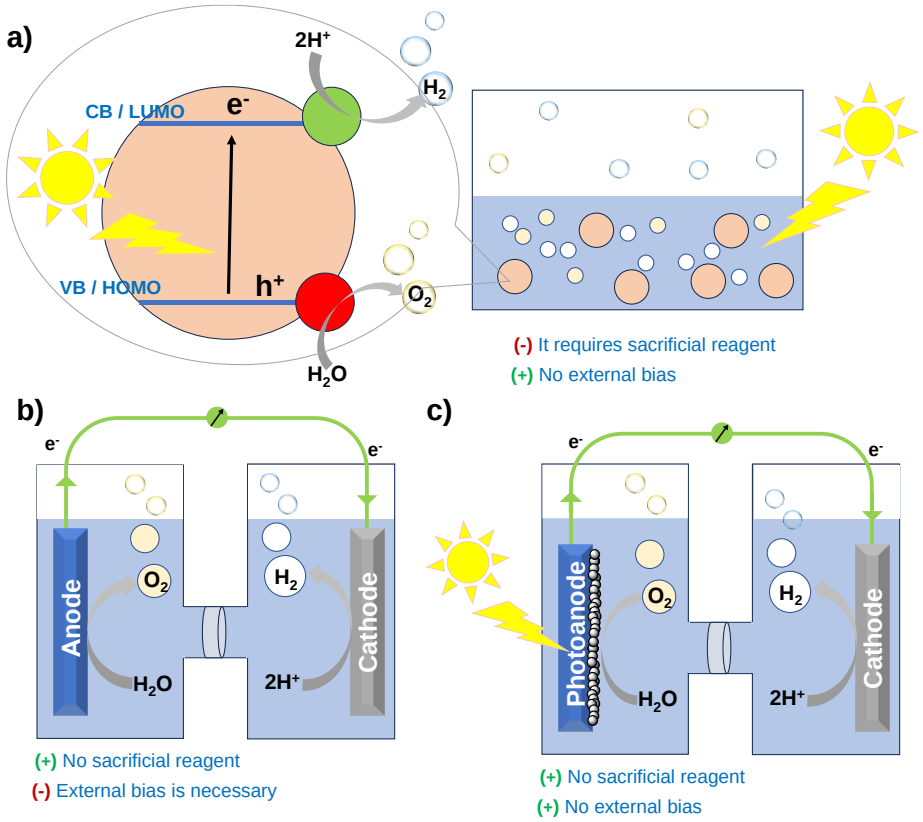

Figure 78 H_2 production from a)photocatalysis b)electrocatalysis c)photoelectrocatalysis

Hydrogen can be produced catalytically from water-splitting, through electrocatalysis, photocatalysis or photoelectrocatalysis. Electrocatalytic hydrogen evolution reaction (HER) involves two different processes for the hydrogen formation from the reduction of protons on the catalytic sites. At first, proton reduces to hydride species on catalytic centers. For the first mechanism, two hydride species react and release a hydrogen molecule, while in the second mechanism a hydride specie reacts with a proton-electron couple releasing a hydrogen molecule[48].

On the other hand, in photocatalysis, there is no external bias required. The initial step involves light absorption from the molecular or the photocatalytic component. Then, electrons are excited to the LUMO orbital or the CB respectively, while holes are left behind in the HOMO orbital or the VB respectively. To optimize the photocatalytic performance, a photosensitizer with appropriate HOMO-LUMO gap or band gap is required so that solar energy is absorbed, it has efficient charge carrier separation and active sites on the catalyst surface.

However, the drawback of photocatalysis is the necessity of a sacrificial electron donor (SED) can be overcome through photoelectrocatalysis. The electrons are provided by an oxidative catalytic transformation at the photoanode over an external circuit to the cathode, where the hydrogen is produced. In analogy to the electrocatalysis, the "external bias" which overcomes the energy barrier is provided by solar excitation.

2D materials can be used to enhance the photocatalytic performance of the semiconductor photocatalyst[49]. Graphene related materials (GRM) are exceptional candidates for H_2 production because they have high specific surface area, high conductivity and electron mobility. They can provide adsorption and catalytic sites. Moreover, their high conductivity and electron mobility are helpful for electron capture and migration. In addition, they can suppress the recombination of the photogenerated electron-hole pairs. The photocatalytic performance can be improved by GRM and boost the efficiency of solar energy conversion[50]. In the last years, GRM have been used in graphene based electrocatalytic and photocatalytic H_2-production.

Moreover, materials like porphyrins can also improve the photocatalytic H_2 production by enhancing light absorption and suppressing electron-hole pairs recombining. More active sites are also provided which is also beneficial for the electrocatalysis as previously mentioned. Last but not least, their easily modifiable structure, their high molar absorption coefficient in the visible region and their various interaction mechanisms with materials.

In this work, a laser-induced rGO (LrGO) with porphyrin combination is additionally examined for electrocatalytic hydrogen production.

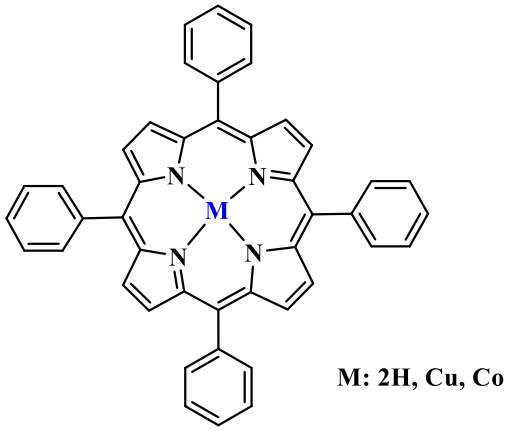

Figure 79 Chemical structures of the molecular porphyrin catalysts used in electrocatalysis in combination with LrGO

Electrocatalytic H_2 production by LrGO

As previously mentioned, LrGO films were given for electrocatalytic H_2 production. Films irradiated with 170fs (444,631,800) and 1ns (258,380,533) were tested. Non irradiated GO film was also tested.

The non irradiated GO film had no current density and showed zero electrocatalytic H_2 production. The results are shown in the Figures below:

(Buffer solution: Na_2HPO_3-NaH_2PO_3 1M, pH=7)

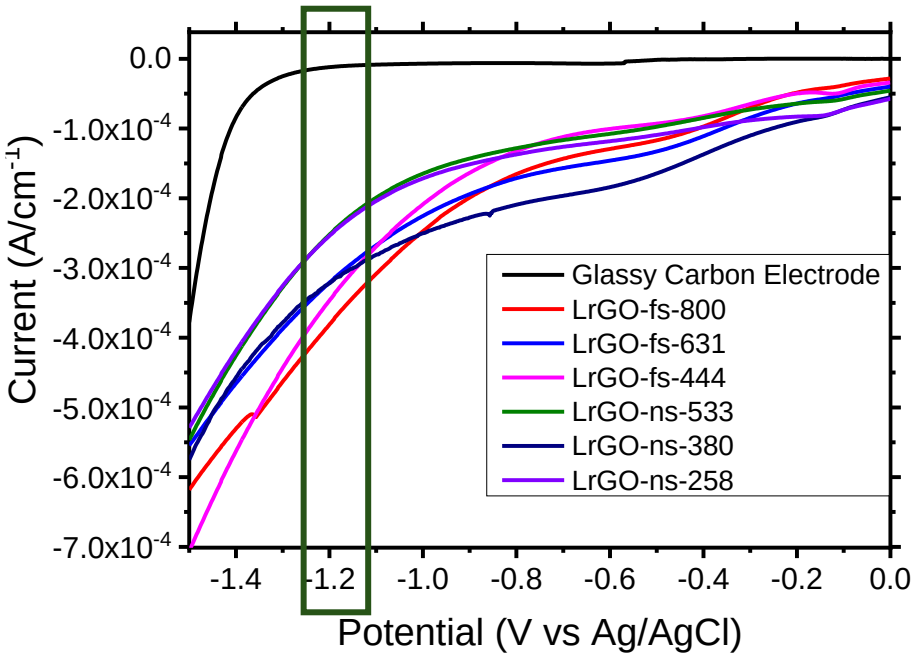

Figure 80 Linear sweep Voltammetry measurements

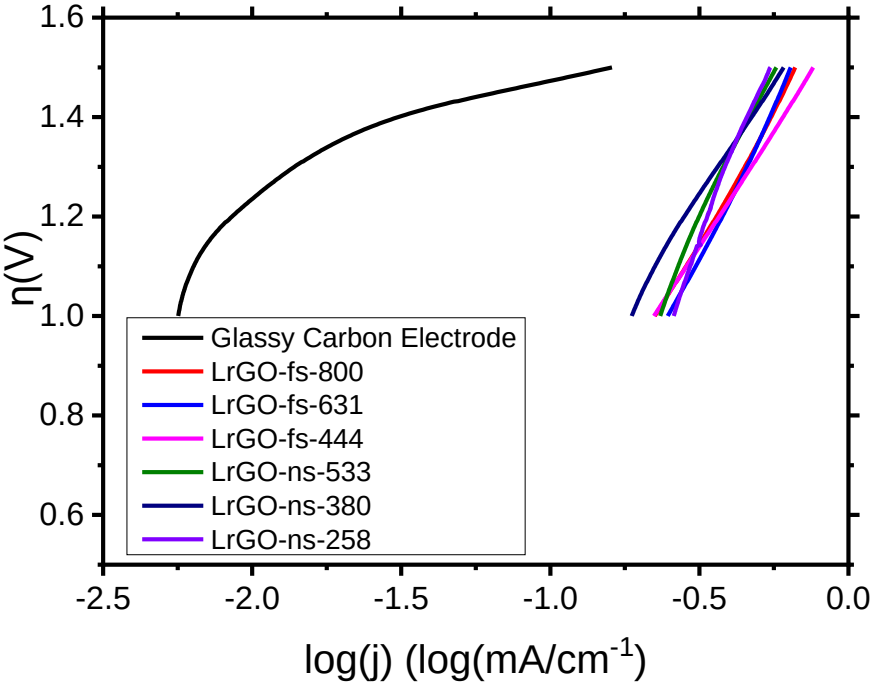

Figure 81 Tafel plots measurements

Electrode	Tafel slopes (V dec^{-1})	E_{onset} vs Ag/AgCl	Current density (μA·cm^{-2})	Overpotential η (V) at 0.5mA*cm^{-1}
Glassy Carbon	0.56	1.2 V	12 at -1.2 V	1.5 V
LrGO-fs-800	**0.98**	**0.65 V**	**381 at -1.2 V**	**1.39 V**
LrGO-fs-631	1.12	0.7 V	321 at -1.2 V	1.46 V
LrGO-fs-444	**0.92**	**0.6 V**	**347 at -1.2 V**	**1.37 V**
LrGO-ns-533	1.35	0.9 V	252 at -1.2 V	1.48 V
LrGO-ns-380	0.92	0.8 V	322 at -1.2 V	1.46 V
LrGO-ns-258	1.74	0.9 V	254 at -1.2 V	1.49 V

LrGO fabricated with 170fs pulses, shows higher current densities. LrGO-fs-444 and LrGO-ns-380 samples show the lowest Tafel slope, meaning they are the most electrocatalytically active. The lowest E_{onset} value is given by the LrGO-fs-444 sample. Thus, the best sample for electrocatalytic H_2 production is the GO film irradiated by 444 170fs-pulses.

Next, the electrocatalysis stability of the above samples are shown below:

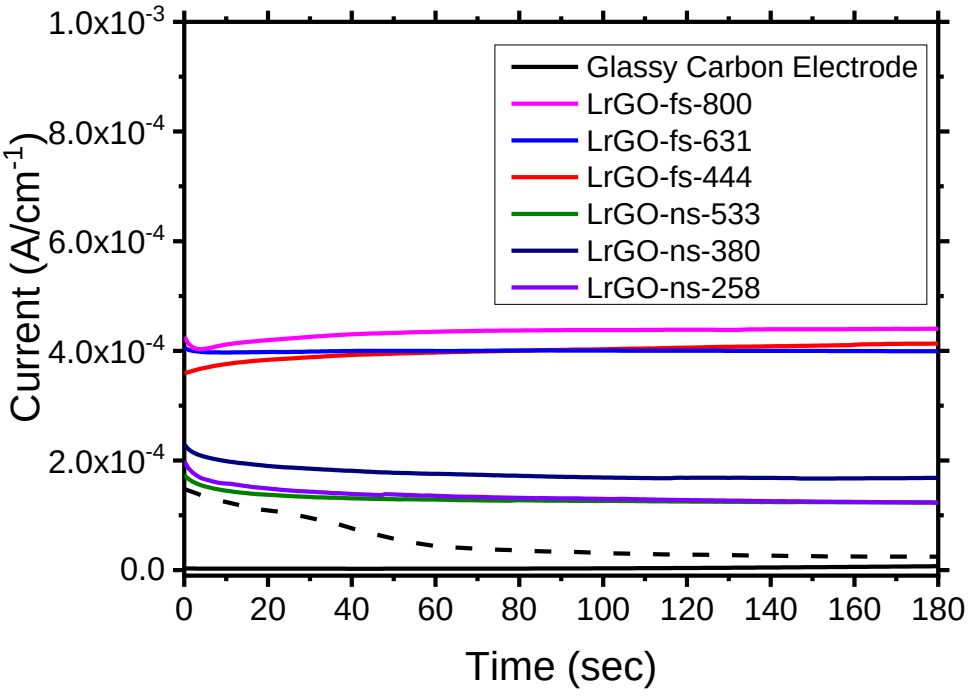

Figure 82 Stability tests at a constant potential -1.2V vs Ag/AgCl applied

Again, the samples irradiated with 170fs pulses show better stability over time. Furthermore, the dashed line corresponds to previously irradiated samples with unoptimized conditions. The unoptimized sample shows significantly worse stability and lower current density.

Conclusion

This master's thesis explores the reduction of graphene oxide (GO) deposited on a glass substrate using pulsed infrared lasers, aiming to identify the optimal reduction conditions for industrial applications such as transparent electrodes and electrocatalytic hydrogen production.

The thesis identifies the best conditions for the reduction of graphene oxide by varying the pulse duration of the infrared lasers. The optimal conditions depend on both the pulse duration and the film thickness (100 nm and 200 nm). The reduction process's effectiveness and the properties of the resulting reduced graphene oxide films are influenced by the initial thickness of the GO films. The study compares the characteristics of films with thicknesses of 100 nm and 200 nm.

Various characterization techniques, including spectroscopy, electrical measurements, and microscopy, provided a comprehensive understanding of the reduced graphene oxide's properties. These methods confirmed the successful reduction of GO and the quality of the resultant films.

The reduced graphene oxide films exhibit properties suitable for many industrial applications. The study highlights their potential use in transparent electrodes and electrocatalytic hydrogen production. This finding underscores the material's potential in energy-related applications.

Overall, this research provides valuable insights into the reduction process of graphene oxide using pulsed infrared lasers, paving the way for its application in various industrial fields. The identified optimal conditions and the demonstrated applications emphasize the significance of this study in advancing the practical use of reduced graphene oxide films.

References

1. Zhu, Y. *et al.* Graphene and graphene oxide: Synthesis, properties, and applications. *Advanced Materials* **22**, 3906–3924 (2010).

2. Xu, Z. Fundamental properties of graphene. in *Graphene: Fabrication, Characterizations, Properties and Applications* 73–102 (Elsevier, 2017). doi:10.1016/B978-0-12-812651-6.00004-5.

3. Cooper, D. R. *et al.* Experimental Review of Graphene. *ISRN Condensed Matter Physics* **2012**, 1–56 (2012).

4. Li, X. *et al.* Graphene films with large domain size by a two-step chemical vapor deposition process. *Nano Lett* **10**, 4328–4334 (2010).

5. Sun, L. Structure and synthesis of graphene oxide. *Chinese Journal of Chemical Engineering* vol. 27 2251–2260 Preprint at https://doi.org/10.1016/j.cjche.2019.05.003 (2019).

6. Dreyer, D. R., Park, S., Bielawski, C. W. & Ruoff, R. S. The chemistry of graphene oxide. *Chemical Society Reviews* vol. 39 228–240 Preprint at https://doi.org/10.1039/b917103g (2010).

7. Gao, W., Alemany, L. B., Ci, L. & Ajayan, P. M. New insights into the structure and reduction of graphite oxide. *Nat Chem* **1**, 403–408 (2009).

8. Hummers, W. S. & Offeman, R. E. *Preparation of Graphitic Oxide*. https://pubs.acs.org/sharingguidelines (1958).

9. Cao, N. & Zhang, Y. Study of Reduced Graphene Oxide Preparation by Hummers' Method and Related Characterization. *J Nanomater* **2015**, (2015).

10. Chen, J., Yao, B., Li, C. & Shi, G. An improved Hummers method for eco-friendly synthesis of graphene oxide. *Carbon N Y* **64**, 225–229 (2013).

11. Pei, S. & Cheng, H. M. The reduction of graphene oxide. *Carbon N Y* **50**, 3210–3228 (2012).

12. Agarwal, V. & Zetterlund, P. B. Strategies for reduction of graphene oxide – A comprehensive review. *Chemical Engineering Journal* vol. 405 Preprint at https://doi.org/10.1016/j.cej.2020.127018 (2021).

13. Chua, C. K. & Pumera, M. Chemical reduction of graphene oxide: A synthetic chemistry viewpoint. *Chemical Society Reviews* vol. 43 291–312 Preprint at https://doi.org/10.1039/c3cs60303b (2014).

14. Kumar, P., Subrahmanyam, K. S. & Rao, C. N. R. *Graphene Produced by Radiation-Induced Reduction of Graphene Oxide*.

15. Zhang, Y. L. *et al.* Photoreduction of Graphene Oxides: Methods, Properties, and Applications. *Adv Opt Mater* **2**, 10–28 (2014).

16. de Lima, B. S., Bernardi, M. I. B. & Mastelaro, V. R. Wavelength effect of ns-pulsed radiation on the reduction of graphene oxide. *Appl Surf Sci* **506**, (2020).

17. Arul, R. *et al*. The mechanism of direct laser writing of graphene features into graphene oxide films involves photoreduction and thermally assisted structural rearrangement. *Carbon N Y* **99**, 423–431 (2016).

18. Trusovas, R. *et al*. Recent Advances in Laser Utilization in the Chemical Modification of Graphene Oxide and Its Applications. *Adv Opt Mater* **4**, 37–65 (2016).

19. Arul, R. *et al*. The mechanism of direct laser writing of graphene features into graphene oxide films involves photoreduction and thermally assisted structural rearrangement. *Carbon N Y* **99**, 423–431 (2016).

20. Sharif, A., Farid, N., Collins, A., Jilani, A. & O'Connor, G. M. Extensive reduction of graphene oxide on thin polymer substrates by ultrafast laser for robust flexible sensor applications. *Appl Surf Sci* **613**, (2023).

21. Picollo, M., Aceto, M. & Vitorino, T. UV-Vis spectroscopy. *Physical Sciences Reviews* **4**, (2019).

22. Akash, M. S. H. & Rehman, K. *Essentials of Pharmaceutical Analysis*. *Essentials of Pharmaceutical Analysis* (Springer Singapore, 2019). doi:10.1007/978-981-15-1547-7.

23. *2.1.2 Reflectance, Transmittance, and Absorption*. (2013).

24. *Duetta™ with EzSpec™ Operation Manual Part Number 5700004252 Rev 1.3*. http://www.HORIBA.com (2019).

25. Adelifard, M. & Darudi, H. A facile fabrication of chemically converted graphene oxide thin films and their uses as absorber materials for solar cells. *Appl Phys A Mater Sci Process* **122**, (2016).

26. Zheng, Q., Li, Z., Yang, J. & Kim, J. K. Graphene oxide-based transparent conductive films. *Progress in Materials Science* vol. 64 200–247 Preprint at https://doi.org/10.1016/j.pmatsci.2014.03.004 (2014).

27. Ράπτης, Κ. Ι. *ΕΘΝΙΚΟ ΜΕΤΣΟΒΙΟ ΠΟΛΥΤΕΧΝΕΙΟ ΣΧΟΛΗ ΕΦΑΡΜΟΣΜΕΝΩΝ ΜΑΘΗΜΑΤΙΚΩΝ ΚΑΙ ΦΥΣΙΚΩΝ ΕΠΙΣΤΗΜΩΝ ΤΟΜΕΑΣ ΦΥΣΙΚΗΣ Συμπληρωματικές Σημειώσεις Για Το Εργαστήριο «Φασματοσκοπία Raman" Του Μαθήματος «Μέθοδοι Χαρακτηρισμού Υλικών» ΑΘΗΝΑ 2016*. http://users.ntua.gr/yraptis/.

28. Gardiner, D. J. *Introduction to Raman Scattering*.

29. Hess, C. • *Basic Principles-Resonance Raman Scattering-Surface Enhanced Raman Scattering (SERS) • Instrumentation-Spectrometer-Excitation Sources • Raman in Catalysis-In Situ Cells-In Situ Raman (of Working Catalysts)*. (2006).

30. Downes, A. & Elfick, A. Raman spectroscopy and related techniques in biomedicine. *Sensors* vol. 10 1871–1889 Preprint at https://doi.org/10.3390/s100301871 (2010).

31. Kymakis, E., Savva, K., Stylianakis, M. M., Fotakis, C. & Stratakis, E. Flexible organic photovoltaic cells with in situ nonthermal photoreduction of spin-coated graphene oxide electrodes. *Adv Funct Mater* **23**, 2742–2749 (2013).

32. Huang, L. *et al.* Pulsed laser assisted reduction of graphene oxide. *Carbon N Y* **49**, 2431–2436 (2011).

33. Ferrari, A. C. Raman spectroscopy of graphene and graphite: Disorder, electron-phonon coupling, doping and nonadiabatic effects. *Solid State Commun* **143**, 47–57 (2007).

34. Hidayah, N. M. S. *et al.* Comparison on graphite, graphene oxide and reduced graphene oxide: Synthesis and characterization. in *AIP Conference Proceedings* vol. 1892 (American Institute of Physics Inc., 2017).

35. Ghorbani, M. M. & Taherian, R. Methods of measuring electrical properties of material. in *Electrical Conductivity in Polymer-Based Composites: Experiments, Modelling, and Applications* 365–394 (Elsevier, 2018). doi:10.1016/B978-0-12-812541-0.00012-4.

36. Gutiérrez, M. P., Li, H. & Patton, J. *Thin Film Surface Resistivity*.

37. Vernon-Parry, K. D. *Scanning Electron Microscopy: An Introduction*.

38. Ul-Hamid, A. *A Beginners' Guide to Scanning Electron Microscopy*.

39. Zhou, W., Apkarian, R. P., Lin Wang, Z. & Joy, D. *Fundamentals of Scanning Electron Microscopy*.

40. Inkson, B. J. Scanning Electron Microscopy (SEM) and Transmission Electron Microscopy (TEM) for Materials Characterization. in *Materials Characterization Using Nondestructive Evaluation (NDE) Methods* 17–43 (Elsevier Inc., 2016). doi:10.1016/B978-0-08-100040-3.00002-X.

41. Eaton, P. & West, P. *Atomic Force Microscopy*. *Atomic Force Microscopy* (2010). doi:10.1093/acprof:oso/9780199570454.001.0001.

42. Wang, S., Lu, A. & Zhong, C. J. Hydrogen production from water electrolysis: role of catalysts. *Nano Convergence* vol. 8 Preprint at https://doi.org/10.1186/s40580-021-00254-x (2021).

43. Li, Y., Wei, X., Chen, L. & Shi, J. Electrocatalytic Hydrogen Production Trilogy. *Angewandte Chemie - International Edition* vol. 60 19550–19571 Preprint at https://doi.org/10.1002/anie.202009854 (2021).

44. Li, Y.-C. *et al.* Graphene oxide-based micropatterns via high-throughput multiphoton-induced reduction and ablation. *Opt Express* **22**, 19726 (2014).

45. Childres, I., Jauregui, L. A., Park, W., Cao, H. & Chen, Y. P. *RAMAN SPECTROSCOPY OF GRAPHENE AND RELATED MATERIALS*.

46. Zhao, Y. *et al.* Self-supported electrocatalysts for high-current-density water/seawater electrolysis. *Journal of Alloys and Compounds* vol. 968 Preprint at https://doi.org/10.1016/j.jallcom.2023.172286 (2023).

47. Afroze, S. *et al.* Solar-Powered Water Electrolysis Using Hybrid Solid Oxide Electrolyzer Cell (SOEC) for Green Hydrogen—A Review. *Energies* vol. 16 Preprint at https://doi.org/10.3390/en16237794 (2023).

48. Zhang, W., Lai, W. & Cao, R. Energy-Related Small Molecule Activation Reactions: Oxygen Reduction and Hydrogen and Oxygen Evolution Reactions Catalyzed by Porphyrin- and Corrole-Based Systems. *Chemical Reviews* vol. 117 3717–3797 Preprint at https://doi.org/10.1021/acs.chemrev.6b00299 (2017).

49. Cao, S. & Yu, J. Carbon-based H2-production photocatalytic materials. *Journal of Photochemistry and Photobiology C: Photochemistry Reviews* vol. 27 72–99 Preprint at https://doi.org/10.1016/j.jphotochemrev.2016.04.002 (2016).

50. Xiang, Q. & Yu, J. Graphene-based photocatalysts for hydrogen generation. *Journal of Physical Chemistry Letters* vol. 4 753–759 Preprint at https://doi.org/10.1021/jz302048d (2013).